DOI: 10.1002/aenm.201702772

Author's version

Device Physics of Hybrid Perovskite Solar cells: Theory and Experiment

Pilar Lopez-Varo, Juan A. Jiménez-Tejada, Manuel García-Rosell, Sandheep Ravishankar, Germà Garcia-Belmonte, Juan Bisquert, and Osbel Almora**

Dr. P. Lopez-Varo, Prof. J. A. Jiménez-Tejada, M. García-Rosell,

Departamento de Electrónica y Tecnología de Computadores, CITIC-UGR, Universidad de Granada, 18071 Granada, Spain

S. Ravishankar, Prof. G. Garcia-Belmonte, Prof. J. Bisquert, O. Almora

Institute of Advanced Materials (INAM), Universitat Jaume I, 12006 Castelló, Spain

E-mail: bisquert@uji.es

O. Almora

Institute of Materials for Electronics and Energy Technology (i-MEET), Friedrich-Alexander-Universität Erlangen-Nürnberg (FAU), Martensstr. 7, 91058 Erlangen, Germany

E-mail: osbel.almora@fau.de

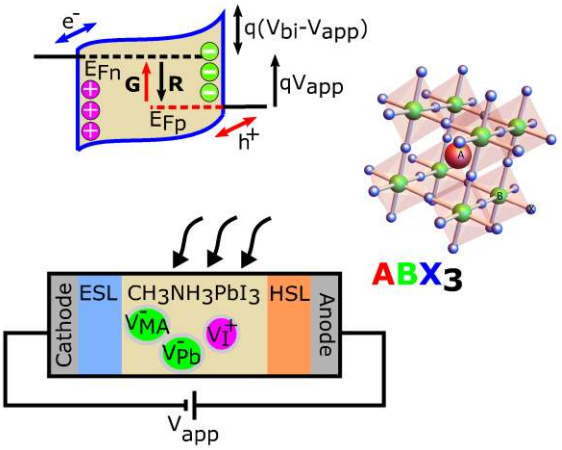

Perovskite solar cells exhibit a series of distinctive features in their optoelectronic response that have a crucial influence on the performance, particularly for long-time response. Here, a survey of recent advances both in device simulation and optoelectronic and photovoltaic responses are provided, with the aim of comprehensively covering recent advances. Device simulations are included with clarifying discussions about the implications of classical drift-diffusion modeling and the inclusion of ionic charged layers near the outer carrier selective contacts. The outcomes of several transient techniques are summarized, along with the discussion of impedance and capacitive responses upon variation of bias voltage and irradiance level. In relation to the capacitive response, a discussion on the $J-V$ curve hysteresis is also included. Although alternative models and explanations are included in our discussion, the review relies upon a key mechanism able to yield most of the rich experimental responses. Particularly for state-of-the-art solar cells exhibiting efficiencies around or exceeding 20%, outer interfaces play a determining role on the PSC´s performance. The ionic and electronic kinetics in the vicinity of the interfaces, coupled to surface recombination and carrier extraction mechanisms, should be carefully explored to progress further in performance enhancement.

Article content

Osbel Almora graduated in Physics from the University of Havana, Cuba, in 2013 and joined the Institute of Advanced Materials of the Universitat Jaume I of Castelló, Spain in 2014. His main topic of interest is the characterization and modeling of energy devices. Most of his research activities have been focused on all-solid-state photovoltaics, including CdTe, perovskite and silicon solar cells.

Juan Bisquert is a professor of applied physics at Universitat Jaume I de Castelló, and the Director of the Institute of Advanced Materials. He has developed the application of measurement techniques and physical modeling that relate the device operation with the elementary steps that take place in the materials and interfaces. He authored a series of books including *Nanostructured Energy Devices* (1. *Equilibrium Concepts and Kinetics*, 2. *Foundations of Carrier Transport*) and 3. *Physics of Solar Cells: Perovskites, Organics, and Photovoltaics Fundamentals* (CRC Press). His current main research interests are perovskite solar cells and solar fuel production.

1. Introduction

Despite the significant advances in power conversion efficiency (PCE), several issues on the characteristic phenomenology of perovskite solar cells (PSCs) are still poorly understood. Among these, one can highlight the diverse time (t) domains of different processes, the corresponding dynamic evolution of charge distributions and the consequent current density-voltage ($J-V$) curves. About the latter, significant debate has taken place on the anomalous hysteresis phenomenon that currently generates some doubts on the actual PCE reports. The main argument here is that for PSCs, the achievement of a well-defined steady state is quite difficult, thus for instance the definition of a reliable short-circuit current density (J_{sc}) or open-circuit voltage (V_{oc}) can be problematic in some cases. Accordingly, typical charge extraction evaluation at short-circuit (SC) or the determination of recombination at open-circuit (OC) are also not so evident.

The study of high efficiency PSCs is accompanied with the analysis of the fundamental physico-chemical mechanisms underpinning their performance. Perovskite solar cells exhibit dynamic hysteresis in their $J-V$ curves[1-3] strongly dependent on the voltage scan rate, direction (from positive to negative bias, or the opposite way), the bias point before a scan, and pre-conditioning treatments (in darkness, or under illumination at open-circuit or short-circuit).[4, 5] They also show a low-frequency giant capacitance response[6, 7] and anomalous experimental transient results,[8, 9] not observed in classical solar cells. Different possible origins of these phenomena have been proposed: trapping of electrons and holes,[10, 11] mobile ions in the perovskite film[12, 13] and chemical or structural changes in the material.[5, 14] Recently, the slow changes associated with the dynamic hysteresis in PSCs have been attributed to the redistribution of slowly moving ions.[1, 6, 15-17] The atomistic study of the motion of the different particles involved in the internal dynamic of the perovskite (electrons, holes, molecules, ions) also supports this statement.[18] The nature and time scales of these different motions have been quantified with the combination of first-principle and multiscale

material modeling and experimental techniques, such as neutron diffraction measurements, quasi-elastic neutron scattering, and ultrafast vibrational spectroscopy.[18]

Different theoretical models and experimental settings assist the interpretation of the effects of ion migration. Macroscopic studies include the analysis of the conductivity, the modeling of dynamic hysteresis[2, 3, 19] or temporal experimental settings such as photovoltage decays[8] or chronophotoamperometry.[6, 9] The type of microscopic mechanisms that intervene in the migration, such as vacancy assisted migration or movement by interstitial ions/defects, and the particular details of their transport through the perovskite are particular topics of study.[20, 21] These studies include the determination of the activation energies for these migration mechanisms using density functional theory,[21] and are compared with kinetic data extracted from the current-voltage response of PSCs.[6] Also, the direct determination of the ion diffusion coefficient has been recently addressed.[22] High-computational studies involving electronic structure, molecular dynamics, and Monte Carlo simulation[20] shed light on the chemical bonding of hybrid perovskites.

The peculiar phenomena that turn out to be ubiquitous in perovskite solar cells make it necessary to adopt a fresh view on physical modeling and measurement that we attempt to summarize in this review paper. Many of the well-established tools and techniques come into question, and specific intuition about central features such as band bending need to be reevaluated. Here we present a first systematic effort to provide a unified picture of the physical modeling and measurement that has been gathered from the initial years of study of the field. Our analysis is far from complete as we believe that the study still needs years of work ahead, and the definite research directions will depend markedly on the ways that materials development of the perovskite solar cell occurs. However, the present work provides a general guideline of studies that were absent in the first years of the perovskite solar cell studies, causing great confusion about the interpretation of physical measurement.

We begin the study with a summary description of the structure, materials, configurations and operation of the perovskite solar cells. These topics are broadly covered in a variety of

review papers and monographies that the reader may consult if more general information is needed. In Section 3, we present a detailed analysis of the physical effects of mobile ions in the solar cell properties. In normal solar cells, it is implicitly assumed that ions form a background fixed charge density, determining the minority carrier. However, new physical effects happen when several types of ions can slowly flow within the device. The notion of doping becomes problematic, the interfaces can experience strong accumulation effects, and the issue needs a careful discussion by simulation that we have explained by separating many cases in order to provide physically based intuition about the energy diagram for interpreting a wide variety of experimental situations.

After exploring the variety of steady-state band diagrams from simulations tools, we summarize in Section 4 the rich phenomenology observed from experimental transient responses. Contrary to that occurring for other photovoltaic technologies, it is clearly stated for PSCs that operating mechanisms spread in time from ns up to tens or hundreds of seconds. While PL transients exhibit rapid decays for the radiative recombination process in the nanoseconds time scale, voltage or current transients present distinct trends with multiexponential decays. Particularly illustrative is the dependence of the voltage decay in open circuit on light-soaking time. The long-time response, in the domain of seconds, is fully altered by the pretreatment signaling the occurrence of dynamically slow ion polarization at the contacts in connection to the charge recombination.

In Section 5, a survey on experimentally gathered impedance and capacitance data is provided. The most intriguing observation, in relation to the solar cell functioning, is the commonly reported light- and voltage-dependent huge values of the low-frequency capacitance (surface capacitance). Its frequency range of observation (seconds) points to the slow transient phenomena treated in Section 4. Again, this is a distinctive feature of PSCs rarely distinguishable in other solar technologies. Dependences of the surface capacitance on perovskite layer thickness and irradiance level allows connecting it to specific ionic or electronic accumulation mechanism at the outer interfaces.

Finally, the issue of the $J-V$ curve hysteresis is extensively addressed in Section 6. This topic attracts continued interest, due both to the significance of this phenomenon for practical operation of the solar cell, and to the variety of phenomena that may act for the delayed and variable response. A summary of the phenomenology on hysteresis and classification of the responses is provided in relation to the variation in control parameters such as scan rate, scan step, temperature, pre-biasing and light soaking. Models for hysteresis are explained stressing the consistency of the ionic/electronic charge accumulation at the electrodes (surface polarization model) with the observed responses and impedance analysis. Strategies of hysteresis suppression are also commented upon. We finish with a few remarking conclusions.

2. Structure of perovskite solar cells

PSCs are basically structured as a light harvesting perovskite sandwiched between the electron and hole selective layers. The use of numerous materials has been reported,[23] however the most successful and extensively studied configuration is that shown in **Figure 1**a, where the TiO_2 layer is grown on top of the fluorine-doped tin oxide (FTO)/glass substrate (typically as a mesoporous scaffold on top of a compact layer), then the methylammonium lead iodide $CH_3NH_3PbI_3$ (referred as $MAPbI_3$ in the next) perovskite and subsequently the spiro-OMeTAD (2,2'(7,7')-tetrakis-(N,N-di-p-methoxyphenyl-amine)9,9'-spirobifluorene). The metallic electrodes are often made of gold in order to achieve better connections with the load (R_{Load}), even though other non-precious metals have been also explored.[24] Thus, in this *regular* structure, the light crosses the substrate through the glass and the transparent conducting oxide (TCO), then first through the electron-selective layer (ESL) to be absorbed at the perovskite, leaving the hole-selective layer (HSL) at the end of the light path.

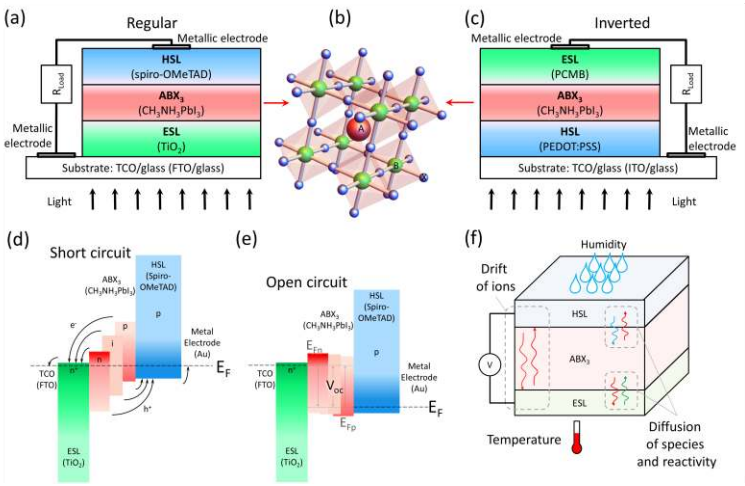

Figure 1. Basic structure of PSCs in (a) regular and (c) inverted configurations. (b) Crystalline structure of perovskite materials in cubic phase ABX_3, where A, B and X are $CH_3NH_3^+$, Pb^{2+} and I^-, respectively, for $CH_3NH_3PbI_3$. General energy band diagram in SC (d) and OC (e) for different possible perovskite conductivities, as indicated, being E_F the equilibrium Fermi lever and E_{Fn} and E_{Fp} the quasi Fermi Levels for electrons and holes, respectively. (f) Main contributing factors in the degradation processes of PSCs. Most used materials in each case are specified in parenthesis. Adapted with permission.[25] Copyright 2017, Sociedad Cubana de Física.

Another important configuration is that of **Figure 1**c, known as an *inverted* structure. Here, in the same light path direction, the sequence of layers is glass/TCO/HSL/perovskite/ESL/metallic-electrode.[26] The selective contacts for these devices are mainly fullerene derivatives and organic compounds, with PCBM ([6,6]-phenyl-C-61-butyric acid methyl ester) and PEDOT:PSS (poly(3,4-ethylenedioxythiophene) doped with *poly(4-styrenesulfonate)*) being the most common ESL and HSL, respectively.

However, irrespective of one or other configuration, $MAPbI_3$ has proved to be the most representative perovskite for photovoltaic applications. As systematically described by Stoumpos et al.,[27] in its high temperature cubic phase, the methyl ammonium organic cation $CH_3NH_3^+$ (MA) is A in the perovskite general formula while the lead and the halogen are B

and X, respectively, with the crystalline structure that of **Figure 1**b. Remarkably, $MAPbI_3$ has an optimum direct band-gap ($E_g \approx 1.6$ eV)[27-30] and the deposition of the material follows easy solution-based fabrication processes, e.g. dip and spin coating,[31, 32] resulting in layers with good crystalline quality at relatively high reaction rates, even when processed at low temperatures. The estimated theoretical PCE for a 500 nm-thick $MAPbI_3$-based single junction solar cell has been calculated to be around 31% with $J_{sc} \approx 26\ \text{mA} \cdot \text{cm}^{-2}$, $V_{oc} \approx 1.3\ V$ and 91% of fill factor (FF).[33]

Importantly, the electrical intrinsic conductivity of $MAPbI_3$ can be modified from p-type to n-type by controlling growth conditions, i.e. by managing the concentration of donor or acceptor shallow defects.[34] For example, recent studies have shown that exposure to excess I_2 vapor pressure can create intrinsic p-type conduction in $MAPbI_3$.[35, 36] This tunable conductivity character has produced a significant scattering in the representation of the energy band diagram of PSCs. While several studies have identified or assumed an intrinsic character of the perovskite, meaning a p-i-n heterojunction, some others suggest p^+-p-n or p-n-n^+ heterojunctions.[25] The two possible energy band diagram situations are illustrated in **Figure 1**d at short-circuit (SC) and in **Figure 1**e for open-circuit (OC) condition. It seems that not gross differences are expected at OC, however at SC, the photocurrent generation is quite sensitive to the nature of minority carriers. Regarding these issues, and including the effects of ions, a more detailed discussion from theoretical modeling by numerical simulations can be found in Section 3.1 to 3.3.

Concerning the general performance, the two other most characteristic perovskites are the hybrid halide $CH_3NH_3PbI_{3-x}Cl_x$ and the formamidinium (FA) cation composed $HC(NH_2)_2PbI_3$.[37] About the former, the chlorine incorporation has been found to mainly improve the carrier transfer across the heterojunction interfaces[38] while in $FAPbI_3$ based devices, a broader absorption toward the infrared region[39] has been obtained.

In addition, one weighty consequence of the PSC structure and involved materials is the

occurrence of significant degradation processes. Despite degradation not being the focus of this review, we briefly mention some important points about this issue in order to support subsequent considerations along the varied discussed phenomena where the reactivity influence cannot be ignored. In Section 5.2 and 6.5, the impact of reactivity mechanisms on capacitance and $J-V$ curves will be noted explicitly. These mechanisms are summarized in **Figure 1**f, with the moisture being the first to be highlighted. $MAPbI_3$ degradation in humid air proceeds by two competing reactions: (i) the generation of a $MAPbI_3$ hydrate phase by H_2O incorporation and (ii) the PbI_2 formation by the desorption of CH_3NH_3I species.[40] Subsequently, loss of $CH_3NH_3^+$ and I^- species and decomposition into $PbCO_3$, $Pb(OH)_2$, and PbO take place.[41] Even if the material is properly encapsulated (or measured in lab conditions under inert atmosphere), devices can still be unstable. Particularly, it has been shown that ionic transport induced by the electrical field can lead to the chemical reactivity of the external contacts with iodide ions.[42, 43] In addition, the temperature can induce decomposition at local temperatures around 100ºC and phase transitions around 57ºC. This is a catalytic factor for the other degradation processes.

3. Numerical simulation of perovskite solar cell devices

Experimental evidence and theoretical models for simultaneous electron and ion transport in the hybrid perovskite materials show that PSCs exhibit characteristics of mixed ionic-electronic conduction. Electronic conduction is quite common and necessary in photovoltaic materials, but facile ion transport by hopping between favorable lattice sites is a less usual characteristic that appears unexpectedly.[44] This effect causes an enormous impact on the understanding of the PSC device operation, as it implies that general properties like the internal band bending, electric field distribution, and carrier injection characteristics at the boundaries with the contacts can have a dynamic change over different timescales under operation. Then, characteristics that are taken for granted in other well-known semiconductor

devices are seen to vary and fluctuate in the PSC. This fact poses a major barrier for understanding and control, as for example, results of many techniques are not reliable, since they depend on details of the measurement protocol. Different distributions of ions inside the perovskite film can alter the electronic operation when illuminated by sunlight. This fact has important implications in terms of the long-term stability[6] as well as the efficiency of the solar cell.[45] For this reason, we begin the review with an analysis of the solar cell device characteristics taking into account the variations caused by the massive displacement of ions.

In perovskite materials, the mobile ionic species are associated with vacancies, ions or interstitial defects.[6] Density function theory (DFT) studies at room temperature on $MAPbI_3$ show the existence of high concentrations of iodide vacancies and methylammonium (MA) vacancies.[46] Some first-principle studies in $MAPbI_3$ perovskites have shown that the most diffusive species (higher mobility) is the I^- anion,[6, 47] and suggest the requirement of a long period of time for the migration of Pb and MA vacancies. This was further supported by theoretical calculations[48, 49] that identified Iodide vacancies as the defect with the lowest formation energy (~0.67 eV) in $MAPbI_3$ similar to values reported by Eames et al.[6]. However, other experimental studies have confirmed the motion of MA^+,[50] with some authors even claiming migration of both I^- and MA^+ ions.[51] Some studies on $MAPbI_3$ suggest an important equilibrium concentration of iodide (I^-), lead (Pb^{2+}) and $CH_3NH_3^+$ (also denoted as MA^+) vacancies, with their respective ions of opposite charge. Other migrating species such as gold[52] or hydrogen[53] have also been detected in perovskite semiconductors.

Therefore, it has been difficult to identify which ions contribute to the strong ionic conductivity observed. However, recent experiments on ionic conduction in perovskites by Senocrate et al.[35] have shed new light on this issue. They first identified that the I^- ion is the dominant long range mobile ionic species (as also corroborated by Li et al.[54] from wide-field PL imaging microscopy) in the perovskite by passing a small current (nA) for one week through a Faradaic cell of type +Cu/$MAPbI_3$/AgI/Ag-, while subsequent XRD measurements showed the only phase change that occurred was the formation of CuI at the Cu/$MaPbI_3$ side.

In addition, they determined no long range diffusion of MA^+ ions, through a similar measurement on a +Pb/$MAPbI_3$/AgI/Ag- cell and tracer diffusion experiments on ^{13}C and ^{15}N enriched $MAPbI_3$ pellets in contact with each other. The authors then measured the evolution of voltage in a dc galvanostatic configuration of a pure $MAPbI_3$ pellet while varying the I_2 partial pressure, allowing for the estimation of the values of ionic and electronic conductivity over a range of partial pressure values. They found that the ionic conductivity reduced with increasing I_2 partial pressure, related to the filling of Iodide vacancies, hence establishing Iodide vacancy migration as the primary mechanism of ionic movement through the perovskite. However, as a generalization, for the steady state analysis, we consider only two ionic species, cations and anions, and assume neutrality of ionic charge in the perovskite as a whole.

Currently, there are two main factors that make ion migration alter the solar cell performance. These two effects will have a protagonist role along our paper, since they will be used for the interpretation of hysteresis in the final part of the paper.

First, the internal electric field created by any biasing voltage, or by the effect of light-induced photovoltage, produces accumulation of ions at the interface contacts.[8] This charge accumulation has a very strong effect on the measured surface capacitance,[55, 56] which is seen to change dramatically depending on the contact material [2, 57] [58, 59]. This mechanism may have a major impact on degradation of the contacts[42] (highlighted in **Figure 1**f). This is because, on the one hand, mobile ions inside the perovskite structure show a very slow motion that progressively adjusts to the variations of voltage. This fact points out a severe influence of the surface polarization on the observed slow dynamic changes in measurement. In addition, the ions accumulated at the interfaces may launch slow electrochemical reactions and even penetrate selective contact material producing severe degradation.[42]

The second effect associated with ion migration refers to the influence of the electrical field distribution on charge collection. In a perovskite solar cell, a large built-in voltage could be expected, and this original voltage can be modulated by the ion drift, modifying the charge

collection properties,[5, 6, 9, 19] see **Figure 2**. Therefore, the internal electrical field is screened by the ion distribution and the net electric field modifies the value of the photocurrent.

In order to quantify these effects, one needs to address the complex problem of device simulation considering not only usual models combining electrons and holes but additional anionic and cationic species that can be redistributed inside the absorber layer. We will provide a short account of the methods used to deal with these problems and then we present and discuss the most relevant problems based on a specific solution model.

Accurate modelling and device simulations present significant challenges for describing the mixed ionic-electronic conduction. A well-known simulation tool that supports macroscopic studies in PSCs is drift-diffusion (DD) simulation.[19, 47, 60] Nevertheless, not all the DD simulations model the distribution of ions in the same way.[61] DD simulation is usually applied to structures such as the one shown in **Figure 2**a-b or the simplified structure of **Figure 2**c. In these figures, the cathode in contact with the electron selective (hole blocking) layer (ESL) and anode close to the hole selective (electron blocking) layer (HSL) are highlighted. Furthermore, the distance x from the ESL/perovskite interface is indicated, which will be $x = L$ at the HSL/perovskite interface for our purposes.

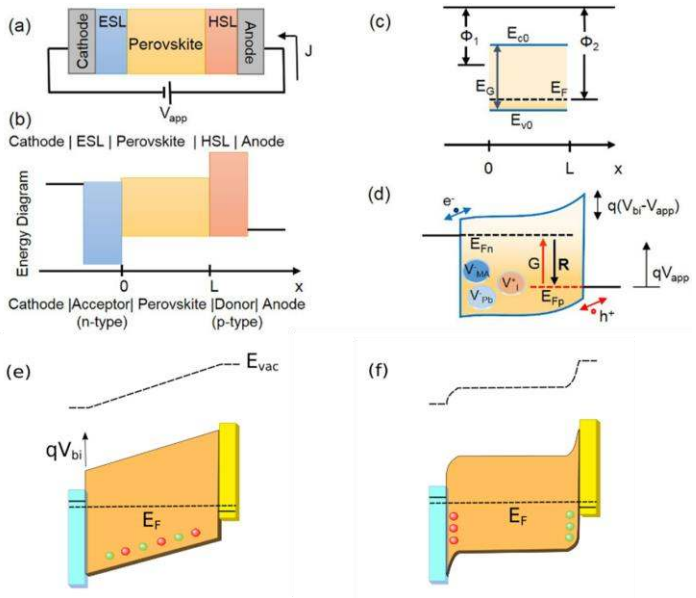

Figure 2. (a) Layers of the PSC: cathode-ESL-perovskite-HSL-anode. (b) Energy diagram of the different layers before contacting. (c) Simplified energy diagram of a p-type solar cell

before contacting in which the effect of the ESL and HSL is incorporated as boundary conditions. (d) Energy diagram for the solar cell under bias voltage V_{app}. Only electrons and holes contribute to the electrical current. (e) Energy diagram of intrinsic perovskite with a built-in potential as shown, establishing an electrical field through the perovskite that is the difference in work functions between the ESL and HSL. The ions (cations and anions are green and red respectively) drift along this electrical field and establish the equilibrium situation of (f), where the shielding of the electrical field through the bulk occurs. Adapted with permission.[3] Copyright 2017, Royal Society of Chemistry.

Some DD simulations consider a steady state ion distribution produced by drift-diffusion mechanisms inside the perovskite, and ion blocking contacts at the perovskite boundaries.[4, 19, 47, 62] In this approach, the drift and diffusion of anions and cations is coupled with the well-known drift-diffusion model for electrons and holes.[8, 19, 47] It is worth mentioning the models proposed by Van Reenen et al.,[62] Richardson et al.,[19] O'Kane et al.,[4] Calado et al.,[47] Gottesman et al.[8] and Neukom et al..[63] Their main differences lie in their approaches of the boundary conditions and the inclusion of different physical-chemical mechanisms in their models. In order to obtain quick simulation approaches, the use of approximate distributions of anions and cations is common practice.[4, 9, 19] Some authors propose that under a net electric field inside the perovskite $(V_{bi} - V_{app})/L > 0$ (V_{bi} is the built-in voltage, given by the difference of contact work-functions, and V_{app} is the external voltage applied between anode and cathode) the positively charge ion vacancies drive into the region of the perovskite adjacent to the HSL. There, they create a narrow positively charge layer. To maintain the neutrality, a negatively charge layer appears, by depletion of the positive vacancies, in the perovskite near the ESL. These regions of opposite charge are termed Debye layers[4, 19, 60, 64] and resemble a dipolar distribution of charge in which the positive and negative charges are confined in thin layers close to the interfaces,[9, 65] with ionic Debye length[64]

$$L_D = \sqrt{\frac{\varepsilon_r \varepsilon_0 k_B T}{q^2 N}}, \quad (1)$$

where ε_r and ε_0 are the relative and vacuum permittivity, k_B is the Boltzmann constant, T the temperature, q the elementary charge and N is the total density of mobile ions forming the interfacial space charge of the diffuse layer. The band energy structure of the perovskite semiconductor, as seen by charge carriers, is modified electrostatically by the Debye layers, which act to screen the built-in field.[4] At high ion densities, the Debye length is over two orders of magnitude smaller than the perovskite width (a few nm compared to hundreds of nm). The inclusion of these thin layers in simulations represents a computational challenge. For this reason, Richardson et al.[19] and O'Kane et al.[4] provided a model that adds asymptotic expressions for the charge in the Debye layers to the DD simulations. In this model, exponential voltage drops are associated with the Debye layers, and a constant compensated electric field is assumed in the bulk between these layers. This model needs further discussion, concerning the important feature of charge accumulation at contact interfaces that explains the giant capacitance as described later.

Other DD simulations incorporate qualitative models, including schematic energy diagrams for the distribution of the compensated electric field in the bulk after the migration of ion vacancies.[6, 9, 66] Authors expect the magnitude of the J_{sc} to be controlled by the extent to which the electric field is screened.[5, 6] Tress et al.[5] solved the DD equations modifying the built-in voltage in relation to the electric field compensation amount in the bulk. They suggested that the rate-dependent hysteresis observed in *J-V* scans is related to a slow field-induced process that tend to reduce the electric field in the device at each applied voltage, and thus, modify the charge collection efficiencies.[5] In a similar way, Zhang et al.[66] also proposed that the presence of these ions at the interface attracts charge that modifies the energy-band bending. This interface charge affects the value of the photocurrent. In that work, Zhang et al.[66] suggested that the lower the interface charge density, the higher the obtained photocurrent. The aforementioned mechanism suggests that the dynamic change in the

interface charge leads to *J-V* hysteresis. Despite these efforts, a precise quantification of the screening of the electric field in the bulk of the perovskite is lacking. In this regard, we proposed a numerical simulation of a perovskite structure in which mobile ions are present, as further described below.[61]

Another topic under study concerning the ion migration is related to the specific ions that are transported through the perovskite (a further analysis is provided in Section 3.1). Richardson et al.[19] and Calado et al.[47] distinguished between slow ions with a uniform concentration along the perovskite and fast ions that are allowed to move. This assumption must be considered with care in steady state studies, as slow ions with non-zero mobility can also migrate after a long period of time. Neukom et al.[63] suggested not employing uniform ion distributions for slow ions. To cope with this problem, they solved the DD equations in two steps. First, the DD equations for the mobile ions are solved at a preconditioning voltage without considering the influence of electrons and holes. In the second place, the DD equations for electron and holes are solved using the previous steady state ion distribution as a fixed variable.

In this work, we have systematically analyzed how the distributions of mobile ions and their vacancies affect the distribution of the internal electric field of PSCs under illumination (**Figure 2**a). Intrinsic and p-doped absorber layers have been analyzed in order to shed light on the nature of the electric field and charge distributions in the perovskite semiconductor.[61] Mechanisms such as capacitive currents, trapping at the interfaces and electron-hole recombination in different layers will be ignored here and discussed in later sections.

The distributions of ions have been determined in steady state by numerically solving the DD transport equations (Supporting Information). The resulting solution for the distribution of ions is useful to interpret experiments in which the bias and illumination conditions are set constant for a long period of time. A second distribution of ions, considered as a heuristic approximation to the exact steady state distribution of ions,[3, 9] is also studied. This second distribution of ions consists of two layers of opposite charge located close to the interfaces,

resembling a dipolar structure similar to Debye layers mentioned previously. All the model equations and detailed description of calculations are presented in Supporting Information.

3.1. Effect of ionic species on the energy diagram of PSCs

In this section, the effect of the migration of one or two types of ions is analyzed. The starting ion distribution can be different from one to another dynamic experiment, and thus alter the interpretation of the experimental results. In order to study different possible scenarios, the following distributions for the cation $c(x)$ and anion $a(x)$ densities are considered.

(i) $a(x) = c(x) = N_{ion}$: ions are fixed and uniformly distributed. They are not allowed to move. The net ion charge density is zero. This is equivalent to consider no ions at all.

(ii) $a(x) = N_{ion}$: the anion concentration is fixed and uniform. Only cations are allowed to move.

(iii) $c(x) = N_{ion}$: the cation concentration is fixed and uniform. Only anions are allowed to move.

(iv) Both types of ions are allowed to move.

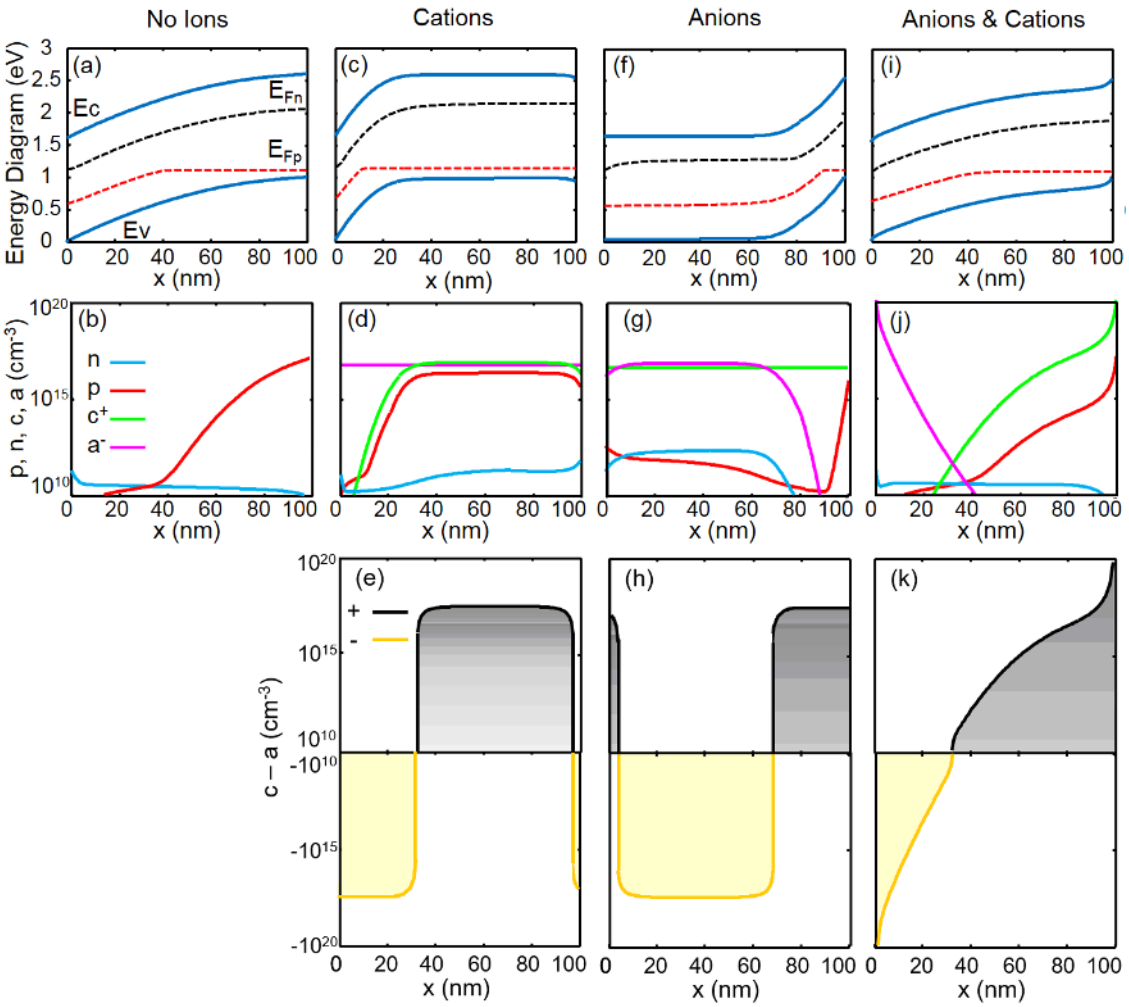

Figure 3. Energy diagrams, charge concentration and net distribution of ions along a p-type PSC with acceptor density $N_A = 10^{17}$ cm^{-3} and average density of ions $N_{ion} = 5 \times 10^{17}$ cm^{-3}, at short-circuit ($V_{app} = 0$ V): (a)-(b) case (i) no ions; (c)-(e) case (ii) only cations move and the anion concentration is uniform; (f)-(h) case (iii) only anions move and the cation concentration is uniform; (i)-(k) case (iv) both ions move. The physical parameters used in the simulations are in Supporting Information.

The distributions of carriers, band bending, and internal electric field in steady state illuminated devices, calculated by DD method indicated in Supporting Information, for p-type PSCs at short-circuit condition are shown in **Figure 3**. The parameters used in the simulation are in Table S1. If only one type of ion is allowed to move, the resulting net distribution of

ions shows two uniform regions with opposite ionic charge (a positive layer at the anode and a negative one at the cathode) (**Figure 3**e,h). The net distributions of ions in **Figure 3**e,h are very similar. A very thin layer of negative charge inside the positive region close to the anode in **Figure 3**e, and a very thin layer of positive charge inside the negative region close to the cathode in **Figure 3**h are also observed. The origin of these thin layers comes from the small difference between the average ion-concentration N_{ion} and the acceptor concentration used in the simulation. These tiny regions can be eliminated if the ratio between N_{ion} and the acceptor concentration is increased. This is seen in **Figure 4**a-b where $N_{\text{ion}} = 10^{18}$ cm^{-3}.

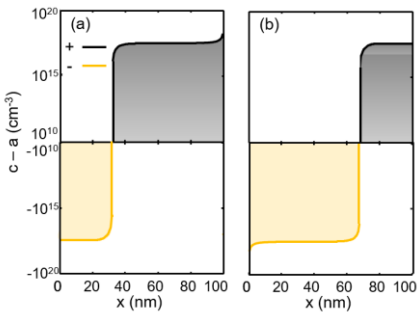

Figure 4. (a), (b) Net ion charge density $c - a$ along a p-type PSC at short-circuit with acceptor density $N_A = 10^{17}$ cm^{-3} and average density of ions $N_{\text{ion}} = 10^{18}$ cm^{-3}, ($V_{app} = 0$ V) when only one type of ions moves (cases (ii) and (iii)).

If both type of ions move (**Figure 3**j-k), again, the positive ionic charge is displaced towards the perovskite-HSL contact and the negative one towards the ESL. However, the resulting net distribution of ions show thin layers where ions accumulate close to the interfaces. The accumulation of ions at the interfaces is combined with an accumulation of free charge of the same sign (holes at the HSL contact). This is an important result in order to explain the experimental observation of accumulation capacitance not only at open circuit but also at short circuit (commented later on, Ref. 144). In particular, we have observed that anions and holes accumulate close to the HSL-perovskite contact at short-circuit (**Figure 3**i)

and the same species close to the ESL in open-circuit (**Figure S2** in Supporting Information). In both cases electronic charge is accompanied by accumulation of ionic charge of the same sign, which contributes to the slow time response observed.

These different distributions of ions have a clear influence on the distribution of other electrical variables, which are analyzed below. The effect of these three distributions of ions on the energy diagrams is similar to increasing the dopant concentration in the device. They reduce the initial width of the depletion region seen in **Figure 3**a. The energy diagram of **Figure 3**c is similar to a highly p-doped semiconductor. The energy diagram of **Figure 3**f is similar to a highly n-doped semiconductor, although no additional electrons are created. **Figure 3**i shows a similar band diagram to that of **Figure 3**a. However, a stronger accumulation of holes at the perovskite-HSL contact can be observed in **Figure 3**i-j in comparison with **Figure 3**a-b. Results at open-circuit condition for the same situations are shown in Supporting Information.

3.2. Effect of the type of semiconductor conductivity

In this section, the analysis made for p-type PSCs at short- and open-circuit steady states is repeated for intrinsic PSCs. In this comparison, we consider that both anions and cations are allowed to move. For consistency, the same simulation parameters are used, including the same values for the metal-perovskite contact barriers (a rectifier contact at the cathode and an ohmic contact at the anode). This study is important to clarify open questions about the nature of the perovskite semiconductor.[3, 8, 61] In particular, we discuss whether the electric field penetrates uniformly into the bulk semiconductor or not. According to our calculations, similar results are extracted in both p-type and intrinsic cases (**Figure 5**). No compensation of the internal electric field is seen in any region in the two cases, despite some suggestions of an electric field compensation at short-circuit operation due to the accumulation of ions at the interfaces.[3, 5, 6, 9] Intrinsic and p-type PSCs are also compared at open-circuit after, observing no differences between these two cases (**Figure S3** in Supporting Information). In the rest of

this work, we consider a p-type perovskite and the presence of both anions and cations in agreement with recent works in which the electronic transport is attributed to holes and the ionic transport to the iodide ions and their respective vacancies.[35, 36, 54]

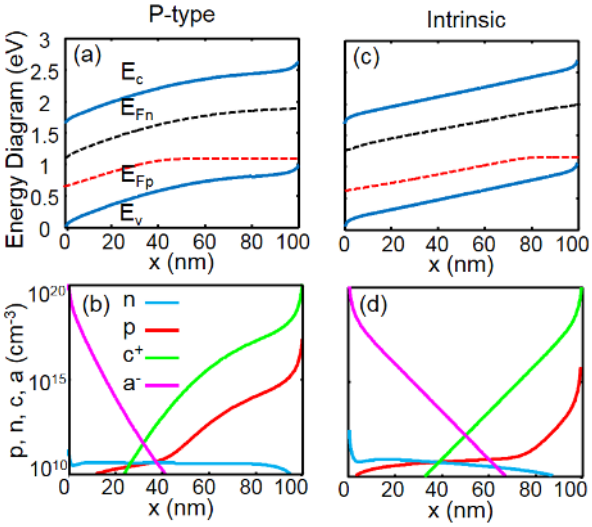

Figure 5. Comparison of energy diagrams (a), (c) and charge densities (b), (d) in p-type and intrinsic solar cells at short-circuit ($V_{app} = 0$ V). Both anions and cations are allowed to move in the device.

3.3. Dipolar distribution of ions

In the previous section, we have seen that different distributions of ions in a PSC produce different distributions of electric field inside the semiconductor, leading to different performances of the device. In this section, the DD distribution of ions (or exact steady state distribution) is compared to a dipolar ion distribution. This dipolar distribution can be considered as an approximation of the first one (**Figure 3**), as shown in the bottom panels of **Figure 6**. This is a usual approximation found in the literature in order to obtain quick simulation approaches.[4, 9, 19] The electric field, band bending and charge densities in illuminated devices are determined for different dipolar distributions. Finally, a comparison with the results obtained with the DD distribution is made.

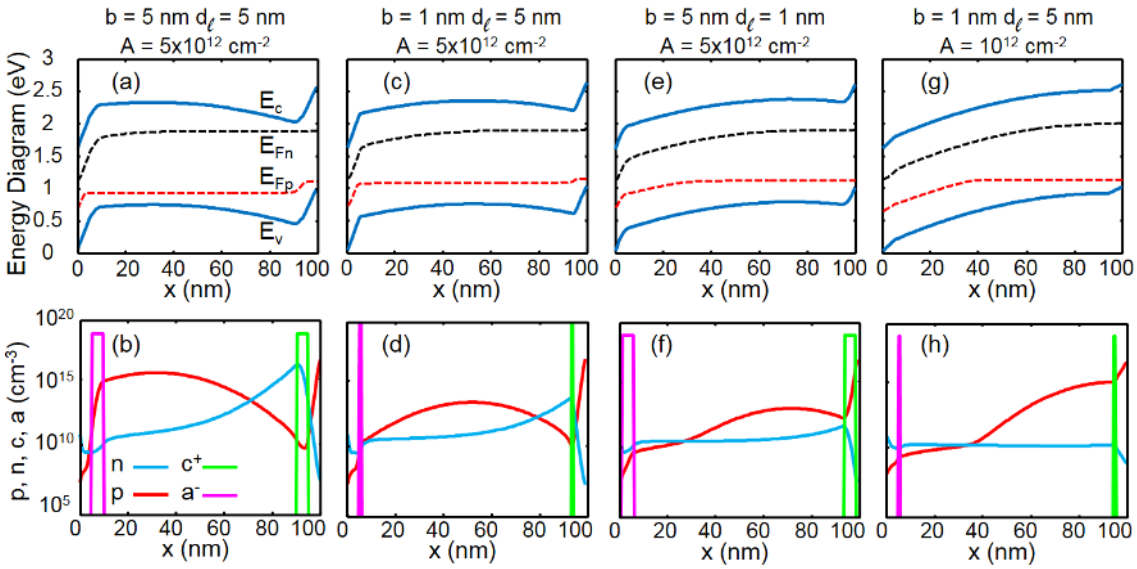

Figure 6. (a), (c), (e), (g) Energy diagrams and (b), (d), (f), (h) charge concentration of electrons, holes, anions and cations at short-circuit with the physical parameter values depicted above the figures.

The sign of the charges in the thin layers is assigned in agreement with the sign of the charge found close to anode and cathode in the DD distributions at short-circuit and open-circuit, as described in detail in Supporting Information. As mentioned before we have anions accumulate close to the anode at short-circuit and close to the cathode in open-circuit. Cations accumulate close to the opposite contact.

Here, we study three cases by changing one of the three parameters and keeping the other two of them constant: (i) the thickness of the sheets b, (ii) the distance of the layers to their closest interface d_l, and (iii) the value of the ion density per unit area A.

Figure 6 shows the results of the numerical simulation of a PSC at short-circuit for different values of b, d_l and A. Two regions within a distance $b+d_l$ to the contacts act as a planar capacitor of thickness $b+d_l$. In each contact region, a voltage $V_{contact}$ drops. In the central region, a voltage V_{bulk} drops. The effect of varying the thickness b, case (i), can be analyzed after the comparison of **Figure 6**a-b and **Figure 6**c-d. We observe that the higher the value of b is, the higher the value of $V_{contact}$ drops along the contact region and the lower the

value of V_{bulk} drops along the bulk (**Figure 6**a). The similar electric field close to the contacts in **Figure 6**a and **Figure 6**c is accompanied with no changes in the charge carrier concentrations within a distance d_l next to the contact regions. In **Figure 6**c, the energy bands are flatter in the bulk, and the carrier concentrations are lower and more uniformly distributed along this central region. Thus, a change in the distance $b + d_l$ (with $A =$ constant) reduces the intensity of the electric field in the bulk, minimizing the effect of the drift mechanism (**Figure 6**c).

The effect of varying d_l (case (ii)) is seen after the comparison of **Figure 6**a-b and **Figure 6**e-f. The bands in the bulk bend in opposite directions in **Figure 6**a and **Figure 6**e. The drifting effect is not only softened but inverted. The cases (i) and (ii) lead to similar conclusions: the displacement of the ionic layers closer to the boundaries is equivalent to making these layers narrower.

Case (iii) analyzes the effect of changing the value of A. The energy diagrams and free carrier concentrations of **Figure 6**g are practically identical to the ones of a perovskite without ions (**Figure 3**a). A similar study with the parameters b, d_l and A of the dipolar distribution for open-circuit is detailed in **Figure S5** (SI).

3.4. Comparison of the DD and the dipolar distribution of ions

One of the main differences obtained for the dipolar distribution is the compensation of the internal electric field in the bulk seen at short-circuit. This is observed in **Figure 6**a,c,e but not in the DD distribution of **Figure 3**i. The ion density per unit area *A* in the dipolar distribution must be decreased (**Figure 6**g-h) in order to achieve similar band diagrams as in **Figure 3**i. The differences between the DD and dipolar distributions seen at short-circuit can also be observed at reverse voltages. An example is in **Figure 7** where the DD and dipolar distribution cases are compared at deep reverse bias $V_{app} = -1\,V$. At this voltage, the ions

tend to accumulate closer to the contacts than at $V_{app} = 0\,V$ (**Figure 3**j).

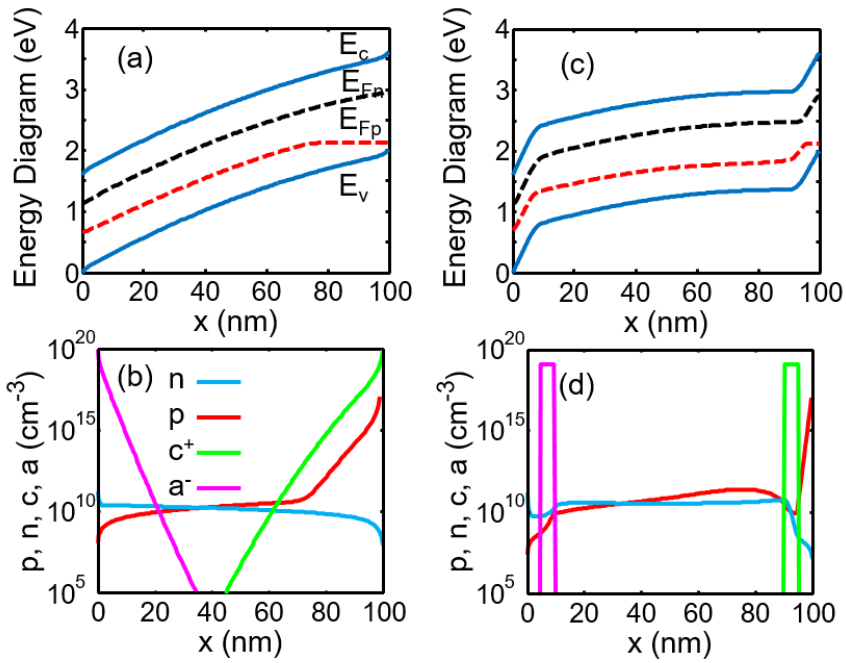

Figure 7. Energy band diagram and distributions of ions, electrons, and holes for a p-doped PSC under illumination at $V_{app} = -1\,V$, (a, b) including drift-diffusion of ions in the numerical simulation and (c, d) assuming a fixed dipolar-distribution of ions in the numerical simulation.

The other interesting feature for the dipolar distribution is the existence of an electric field located in the bulk of the absorber layer that opposes the internal electric field at short-circuit **Figure 6**a,c,e and not existing in **Figure 6**g. The electric field seen in the bulk of **Figure 6**a,c,e facilitates the collection of charge at the electrodes, thus increasing the photocurrent close to the short-circuit region. As mentioned before, some authors suggest that ionic charge accumulates at the edges of the perovskite in the Debye layers.[4, 19] From this comparative analysis (**Figure 3** and **Figure 6** for short-circuit, **Figure 7** at $V_{app} = -1\,V$, and SI for open-circuit) the surface band bending associated with Debye layers is detected only in the dipolar

distribution of ions (**Figure 6** and **Figure 7**c). For the DD distributions of ions, the bands bend very slightly close to the perovskite interfaces (**Figure 3**i and **Figure 7**a), not showing this Debye layer.

It is immediately apparent that the distribution of the ions and carriers for the DD and dipolar distributions will have a strong impact on the device performance. The large neutral region in the bulk of **Figure 6**a,c,e shows that the photogenerated carriers in the bulk will be separated mainly by diffusion to the contacts, as opposed to **Figure 3**i where the ions create their own electrical field through the device, which facilitates charge separation similar to the case without ions. The charge extraction at the contacts in both cases (DD and dipolar distributions) should also be different. In the case of the dipolar distribution, steep potential drops at the contacts can serve as preferential recombination sites for photogenerated carriers (surface recombination), and indeed this is often used to explain the large reduction in open-circuit potential when scanning from short-circuit to open-circuit.[3]

It must also be noted that these Debye layers provide large injection-extraction barriers for the carriers, and consequently, the device performance is mostly controlled by the efficacy of charge extraction and recombination at the contacts itself rather than any transport considerations.

Overall, the approximation of the exact steady state ion distributions by means of dipolar distributions is a reasonable starting model, but it must be used carefully because changes in the parameters that determine the dipolar distribution of ions affect the net distribution of electric field in the perovskite semiconductor significantly.

Another important conclusion is about the discussion of the general doping character of the hybrid perovskite and the basic energy diagram model, i.e. whether the barrier is close to one interface, or the built-in voltage produces a slanted band as in a p-i-n solar cell. Our calculations show that so far as the moving ion density is significant and close to the native doping density, the moving ions determine the barrier and field distribution irrespective of the conductivity nature of the perovskite, such as p-type or intrinsic semiconductor. Therefore,

one needs be aware that pretreatments of the device may produce important and sometimes irreversible changes in the operation of the solar cell, as shown experimentally.[67]

4. Transient response measurements

The physical phenomena occurring in a perovskite solar cell span an impressive range of diverse timescales, from the phonon response for charge shielding and cooling of photogenerated carriers in picoseconds time to the slow relaxation at room temperature that may take seconds. In the next sections of this review, we will describe a variety of techniques which are used to probe the different phenomena that occur in the slow side of the general time scale, i.e. from microseconds to seconds. Time transient experiments as well as frequency domain techniques are surveyed. Here, we aim to bridge the gap between fundamental properties and device operation. Therefore, we need to measure full devices with contacts and determine the observations corresponding to different relevant phenomena such as transport, recombination, charge injection and ion drift, identifying if possible the locus of the physical signal, i.e. the bulk of the absorber, grain boundaries, or outer interfaces. We present a selection of important descriptions and explanatory experiments approaching central aspects of the unique phenomenology of PSCs. With this purpose, we first comment on methods of transient time measurements at different time scales, as well as the consideration on recombination. Subsequently, in Section 5, our attention will be focused on the charge accumulation by discussing the capacitance (C) with the associated resistance (R). In our program to cover the main aspects of the device operation for practical purposes, the hysteresis of $J-V$ curves plays a dominant role and this issue will be approached in Section 6.

4.1. Characteristic response times and basic transient behavior

For characterizing the response time domains and transient behavior of PSCs, several

techniques and particular experiments have been reported in the literature. In general, given the significant variety among device designs (e.g. materials, structure of layers) and fabrication procedures (e.g. composition, variables during processing), certain scattering is often found for most measurements on these devices. However, general features can be highlighted as typical and even unique, especially when samples of large quality and efficiency become available

Obviously, in the focus of our approach, the electron-hole recombination mechanisms play a fundamental role. These are (i) the radiative recombination and the non-radiative (ii) Shockley-Read-Hall (SRH) and (iii) Auger recombinations. While in the first case a photon is emitted, in the SRH recombination, the electron relaxation is assisted by midgap states (traps) and the energy is dissipated as lattice vibrations. In the other case, the Auger recombination occurs when the energy is given to a third carrier, which accesses a different kinetic energy in the same band and then is often thermally relaxed.

It should be noticed that the absorption coefficient α of $MAPbI_3$ is quite remarkable for having an unusually sharp shoulder near E_g with higher values than most other comparable semiconductors, which can be observed in **Figure 8**a. This abrupt optical band edge exhibits a clear exponential law $\alpha \propto \exp[h\nu / E_U]$ with the photon energy $h\nu$. The resulting Urbach tail energy $E_U = 15$ meV is far lesser than a-Si and CIGS solar cells. Actually, it approaches those of other successful direct-band-gap materials such as GaAs and CdTe.[68, 69] Therefore, contrasting indirect-band-gap materials like a-Si, the low E_U of $MAPbI_3$ suggests a very low degree of structural disorder and the purely exponential Urbach tail means that no optically detectable deep states are present in the $MAPbI_3$ material. This is a key element for explaining the large achieved V_{oc} values around 1.1 V, whose non-radiative losses has been estimated around 230 mV from the radiative V_{oc} limit of 1.33 V.[70]

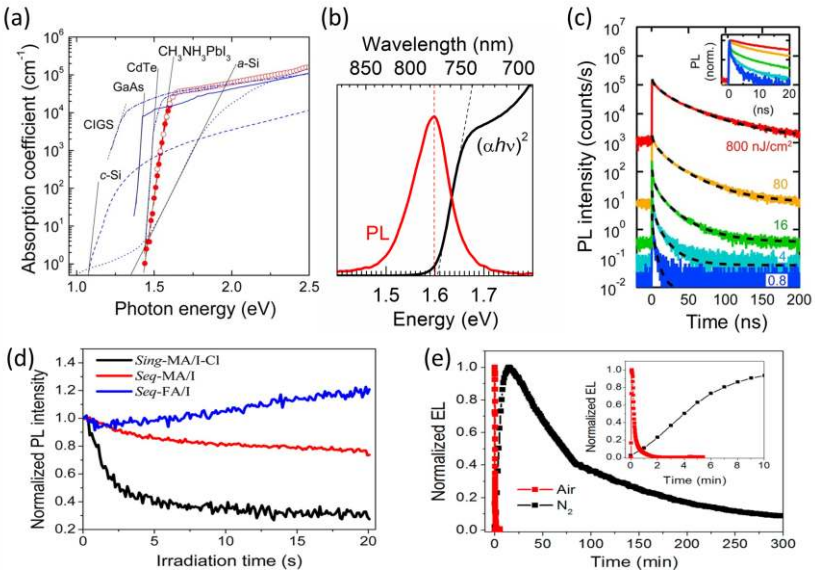

Figure 8. (a) Absorption coefficient spectra of high quality semiconductors in photovoltaic technologies, as indicated. Adapted with permission.[68] Copyright 2014, American Chemical Society. (b) PL spectrum and corresponding absorbance (in Tauc plot representation for direct band-gap recombination) of a TiO_2/$MAPbI_2$ layer showing virtual absence of Stokes shift around the band-gap: 1.6 eV (775 nm). Data courtesy of Thi Tuyen Ngo (INAM). (c) PL decays from different pulsed fluences in a $MAPbI_3$-based device. Adapted with permission.[71] Copyright 2017, American Chemical Society. (d) Evolution of normalized PL intensity under continuous excitation for three different devices of distinct perovskite and fabrication procedure. Reprinted with permission.[17] Copyright 2014, American Chemical Society. (e) Evolution of the normalized EL signal of a working device under air and nitrogen atmosphere at constant voltage (1.5 V). The inset shows the evolution of the signal at a shorter time-scale window. Reprinted with permission.[72] Copyright 2015, American Chemical Society.

The radiative recombination in $MAPbI_3$ is basically due to band-edge electrons and holes, as is evident from the nearly absent difference (at most 10 meV) between the absorption onset and the photoluminescence (PL) peak, i.e. the Stokes shift.[30, 70, 73, 74] This is illustrated in **Figure 8**b where PL and absorbance (in Tauc plot representation) spectra are compared. In contrast, some singularities in alternative perovskites can be mentioned. For instance, in the

work by Wright et al.,[75] the Stokes shift in $FAPbI_3$ was found to be temperature dependent and larger when the excitation fluence was reduced. Moreover, for $CsPbBr_3$ nanocrystals, it is enhanced to hundreds of meV as the nanocrystals edge length are reduced to a few nanometers[76] and even anti-Stokes shift has been found in $MAPbI_{3-x}Br$.[77]

As a basic practice for testing radiative recombination, the samples are typically pulsed with a nearly monochromatic light source and the PL decay is recorded in order to estimate the PL lifetime. For PSCs, these measurements report values from tens to, unusually, hundreds of nanoseconds, extracted from the fitting to a mono-exponential law that characterizes the dominant radiative recombination path. Nevertheless, in some studies, a two-time constant PL decay has been found[78-81] with the consequent consideration of competing recombination mechanisms. In this context, the work by Kanemitsu and co-workers[30] particularly showed that PL decay curves are sensitive to the excitation fluence, as in **Figure 8**c, and that the PL decay dynamics are well explained by the free-carrier band-to-band recombination rather than the exciton recombination. The latter was concluded from the absence of Stokes shift (lack of non-radiative recombination increase) at larger excitation fluences, when the PL decays are faster and two time constants appear. In addition, they also proposed that photon recycling could be the responsible for the unusual slow PL decay.[30]

On the other hand, other singular behaviors were reported by Sánchez et al.,[17] who measured the evolution of the PL intensity under continuous excitation for different device structures and fabrication procedures. Two decaying intensities (Sing-MA/I-Cl and Seq-MA/I in **Figure 8**d) and an increasing one (Seq-FA/I in **Figure 8**a) were noticed. The PL intensity drop, was attributed to the increase of the nonradiative losses, the increase of charge separation rate toward regions such as grain boundaries, abrupt changes in the absorption spectrum of the perovskite upon illumination as a consequence of the dielectric polarization or anisotropic absorption of the different light polarization angles. This latter explanation, upon reaching the dielectric polarization of the device, would be compatible with the slight PL enhancement for the Seq-FA/I sample. Complementary to the reversible PL responses of

Figure 8a, a subsequent study[72] also showed the electroluminescence (EL) evolution with time at a constant applied bias. It was shown that the EL presents a mostly-irreversible increase followed by a quenching in different time scales depending on the atmosphere composition.

Returning to the PL decays from different pulsed excitation intensities, Handa et al.[71] made an interesting combination of these results (fluence dependence of time constants) with photocurrent (PC) measurements, proving a significant reduction of the external quantum efficiency (EQE) above a certain level of illumination. The direct implication here is that the carrier-injection rate is sensitive to the photogenerated carrier density, meaning that a carrier-injection bottleneck strongly enhances recombination losses of photocarriers in the perovskite layer at high excitation conditions. Moreover, they discarded the influence of Auger recombination for photocarrier densities below 10^{17} cm^{-3}.

Additional irregularities were noticed by Unger et al.[15] from their study of full EQE spectrum evolution with time and corresponding J_{sc} change. As displayed in **Figure 9**a, after half an hour, the spectral shape of the EQE did not change substantially between repeated scans, but a vertical shift appeared in correspondence to the current reduction by that time in **Figure 9**b. This suggests that the PC decay results from a reduction in the charge extraction efficiency rather than optical changes to the absorber or contact layer. Consequently, a direct macroscopic implication arises here from these slow transients: a serious unreliability can be found with the matching between integrated EQE values and PC densities determined from $J-V$ measurements, mainly at long delay times or steady state PC measurements. Furthermore, the evaluation of complementary important parameters can be similarly affected for these anomalous behaviors. That is the case, for instance, of the yielded open-circuit voltage radiative limit obtained from EL and EQE, as presented by Tvingstedt et al.[70] and Tress et al..[82]

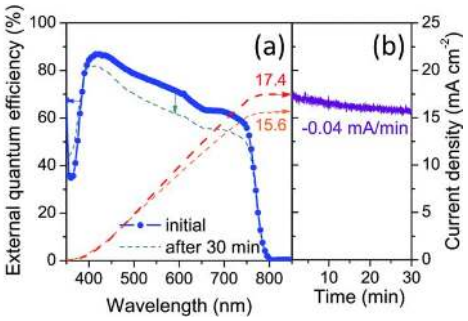

Figure 9. Reversible evolution of EQE spectrum (a) and corresponding J_{sc} (b). Adapted with permission.[15] Copyright 2014, Royal Society of Chemistry.

At this point, it is already clear that the competition of several factors affecting the charge extraction, also evidenced in the radiative recombination, produce a noteworthy time change in recombination, and thus current. Here is precisely where several studies have been focused on, e.g. dealing with the evolution of PC and open-circuit voltage (V_{oc}) under different configurations, perturbation types and devices characteristics. As in **Figure 10**b-d, one basic approach is to apply a light perturbation and record the subsequent response. For instance, in the simplest case, when the sample behaves nearly as an RC circuit (**Figure 10**a), the current at SC should decay exponentially with an extraction time constant $\tau_{ext} = R_{ext} \cdot C_{sc}$ and the voltage at OC with a recombination time $\tau_{rec} = R_{rec} \cdot C_{oc}$. However, as we will comment in the following section, for PSCs it can be quite challenging to actually obtain such "textbook" experimental relaxations.

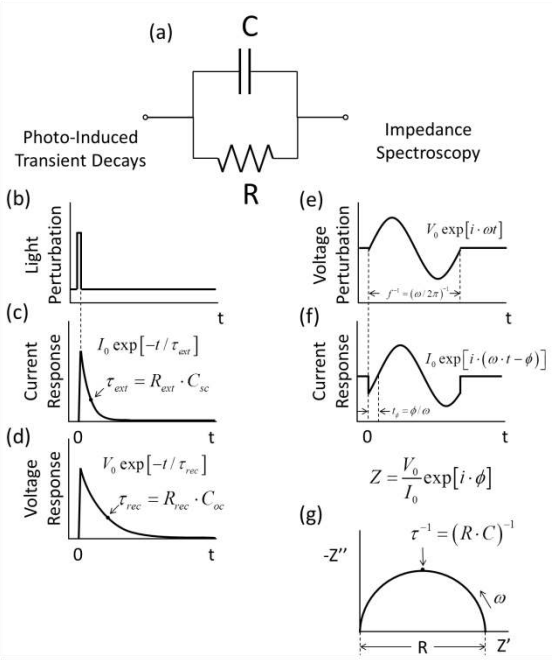

Figure 10. Two different ways to evaluate the characteristic time constant of a sample that ideally behaves like a RC circuit (a): by photo-induced transient decays (b-d) or by impedance spectroscopy (e-g). In each case, the perturbation (above) and the response (below) with time are displayed. Additionally for the IS the corresponding Complex plane plot is shown (f).

Among the most common practices one can find in the reports from several groups are those of photo-induced (PI) transient photocurrents (TPC) and transient photovoltage (TPV), where typically the signal produced by a small light pulse perturbation is recorded in SC and OC conditions, respectively.[83, 84] The main aim of acquiring TPV is to evaluate the lifetime of the charge carriers as a measure of the recombination in the sample, while the TPC provides a quantification of the amount of charge produced by the device given a certain illumination, being evidently the time τ_{rec} (at OC) larger than τ_{ext} (at SC). In addition, a tricky sequenced combination of illuminated OC and dark SC is also often used to measure the charge evolution at a given V_{oc} in the photo-induced charge extraction (PI-CE)[83-85] technique.

A two time constant decay process was first identified in this context by Sánchez et al.[17] by measuring PI-TPV on several configurations. Subsequently O'Regan et al.[86] conducted a

broader description during their studies on PI-TPV, PI-TPC and PI-CE. Illustratively, PI-CE measurements at 1 sun showed a transient photocurrent decay of 180 mA cm^{-2} in about 50 μs (inset of **Figure 11**a) while the remaining 50 $\mu A \cdot cm^{-2}$ needed seconds to relax (**Figure 11**a bottom axis). Importantly, the integrated charge collected for the slow decay (~3.6×10^{-5} $C \cdot cm^{-2}$) was about 50 times higher. Similarly, the PI-TPV decays at 1 sun were found to present a fast component of 1-2 μs and a slow part around 5-10 μs, as observed in **Figure 11**b. Subsequently, further reasoning[87] associated the fastest lifetime from the PI-TPV with recombination processes. They also suggested that reorganization of dipoles could explain the slowest relaxations.

Interestingly, current interrupt voltage measurements were also shown to evolve in the domain of milliseconds, as shown in **Figure 11**c. By switching from illuminated SC to dark OC, the sample voltage rises during ~ 2 ms up to a peak while charge is transported toward the contact electrodes and hence it decays during tens of milliseconds due to recombination.[86] Importantly, the time of SC illumination enhances the V_{oc} peak, possibly indicating that it increases the band offset at the voltage generating interface(s) in the cell. Subsequently, Palomares and co-workers[88] compared the two time constant TPV decays between devices with and without mesoporous TiO_2 and also looked at the transient absorption spectroscopy (TAS)[84] patterns. The results showed apparent differences only for the slowest recombination time and therefore, they assigned the fastest component to recombination between electrons in the $MAPbI_3$ and holes in the HSL.

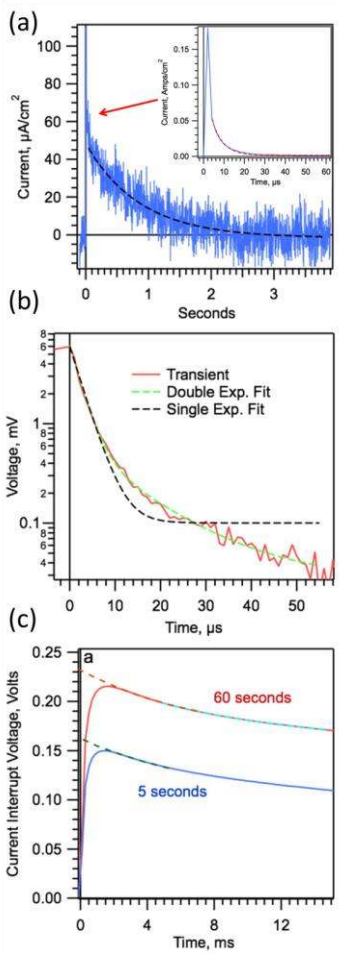

Figure 11. Different transient behaviors showing two time regimes. (a) Current decay from PI-CE set up with the first 60 s of SC (fast transient) in the inset. (b) Experimental PI-TPV and theoretical fitting with mono- or double-exponential relaxation laws. (c) Dark V_{oc} decay following current interrupt from illuminated SC with similar J_{sc} but during different times, as indicated. Adapted with permission.[86] Copyright 2015, American Chemical Society.

4.2. Slower than seconds relaxation processes

Beyond double exponential decays, the work of Baumann et al.[89] identified three distinct time regimes during the V_{oc} decay at OC under several pulsed illumination intensities ranging from 1-100 mW·cm^{-2}. Importantly, while the two first characteristic time constants were of 10-100 μs and 1-100 ms, respectively, the third phase of the decay was as slow as 10 s. As

illustrated in **Figure 12**, this behavior is different from that of organic solar cells (OSCs) whose decays can be fitted to a single exponential along almost the complete transient. In all the cases, the slowest process was associated with shunting and the apparent illumination dependent recombination once more became a target of further discussion keeping in the core of debate the influence of the interface. About the latter, Nagaoka et al.[90] also found similar decays but specifically pointed to the sensitivity to the nature of the perovskite/ESL interface.

Moreover, Bertoluzzi et al.[91] attempted to separately inspect the fast and slow components by measuring short lifetimes with typical PI-TPV (pulsed constant small perturbation with different background illuminations) and the large time constant from V_{oc} decays (switch from light to dark at OC) at different illumination intensities, also known as open-circuit voltage decay (OCVD). Their results corroborated 100 μs and 1 ms for the faster components whose meaning was ascribed to discharge and recombination of photogenerated electrons and holes. However, the third and slowest component, with an estimated characteristic time up to 100 s, was found to behave as a power law decay relaxation. Ionic-electronic polarization and depolarization kinetics depending on internal voltage were proposed as explanation. Importantly, they introduced the useful concept of instantaneous relaxation time defined as

$$\tau_{ir} = \left(-\frac{1}{V}\frac{dV}{dt} \right)^{-1} . \qquad (2)$$

This parameter straightforwardly gives a criterion on the presence or not of exponential relaxation decays and it also illustrates the characteristic time constants or domain.

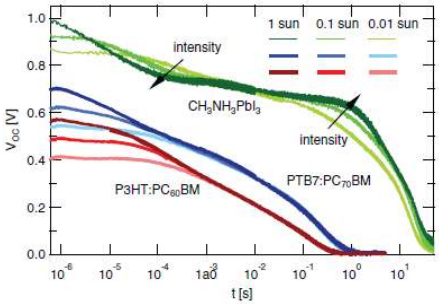

Figure 12. Photovoltage decay of a $MAPbI_3$ based solar cell (green) and two OSCs (red and

blue) for different illumination intensities, as indicated. Differently to OSCs, the PSC decay is divided in three time regimens. Reprinted with permission.[89] Copyright 2014, AIP Publishing in accordance with the CC BY 3.0 license.

Furthermore, the effect of prior light soaking was found to be determinant on the shape of the OCVD, as described in the contribution of Gottesman et al..[8] The two types of OCVD response are shown in **Figure 13**a and the related τ_{ir} are presented in **Figure 13**b, where the differences are evident after the initial fast decay (~1.0-0.8 V) that is out of the resolution of this experiment. Initially, or when dark recovery is set before the pulse, a slow decay of seconds take place when V_{oc} goes from 0.8 V to 0.2 V with the competition between exponential (plateaus in **Figure 13**b) and power law (monotone regions in **Figure 13**b) relaxation decays. Subsequently, an even slower power law relaxation occurs during more than 10 s. Differently, when light soaking is set before the pulse, a faster exponential decay reduces V_{oc} from 0.8 V to 0.2 V with a time constant of 10 ms and the slowest power law relaxation takes at least an hour to remove the remaining electrostatic internal potential ΔV_{elec}. In other words, light soaking (i) makes the initial V_{oc} decay faster but (ii) slows down the final part of the decay where an extra ΔV_{elec} takes considerably more time to relax. Regarding the first issue, the light soaking conditioning of fast recombination was stated in terms of major changes in the contact region deduced from physical simulations. Likewise, other modeling results illustrated that ΔV_{elec} is possibly sustained by the charge accumulation of slow, mobile positive ion charges and electronic holes in a double layer at the perovskite/ESL interface, as shown before in Fig. S2. These results were subsequently corroborated by Hu et al.[92] on diverse device configurations. Additionally, they measured the V_{oc} as a function of the illumination intensity with and without light soaking preconditioning. They observed a clear V_{oc} reduction after light soaking above a given illumination level, which they attributed to

large surface recombination of accumulated electronic carriers at the perovskite/ESL interface upon light soaking.

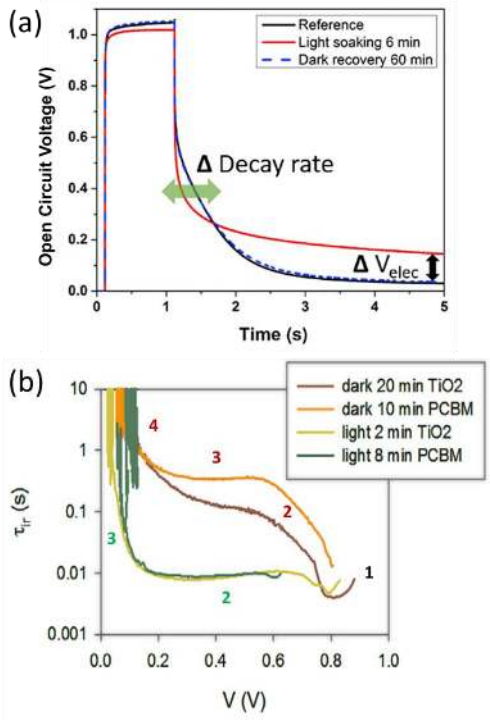

Figure 13. Effect of light soaking in the V_{oc} of PSCs. (a) Dark transient V_{oc} after long term storage in dark (Reference), light soaking (6 minutes), and again dark recovery (1 hour). Reprinted with permission.[8] Copyright 2016, Elsevier. (b) Instantaneous relaxation time from OCVDs similar to those of (a) for PSCs with different ESL and with prior light or dark soaking times, as indicated. During light soaking, at least three time regimens are identified and from dark recovery, the relaxation can be possibly divided in 4 stages, as indicated. Adapted with permission.[91] Copyright 2015, Royal Society of Chemistry.

However, besides light soaking, the polarization history or pre-poling has been found to directly modify the internal processes behind the slow mechanisms too. **Figure 14** shows the J_{sc} after switching from OC to SC under constant 1 sun illumination for two preceding reverse applied voltages measured by Chen et al.[93]. Once more, the separation between faster and slower responses takes place. Independently of poling, a quicker decay occurs in all cases in a time scale from milliseconds to seconds presumably associated with capacitive effects due

to electrode polarization. Afterward, for the transient without poling, the J_{sc} reaches its constant equilibrium level, which is the general shape of the response, although in some reports[6, 90], the possibly capacitive transient can last tens of seconds. In contrast, as the reverse poling increases, a larger reduction of J_{sc} happens that relaxes toward the equilibrium level during about 100 s. This second process could be explained in terms of contact barrier modification due to interface ionic charges. Illustrative of the ionic nature of charge balance at the interfaces, measurements by Almora et al.[64] on $MAPbI_3$ showed a typical Guoy-Chapman diffuse layer performance.

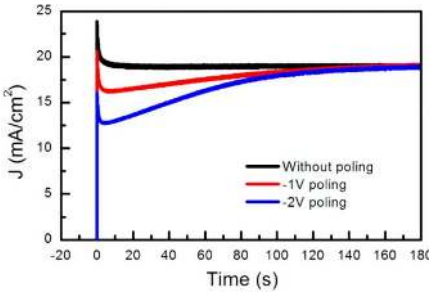

Figure 14. Dynamic J_{sc} transient behavior when switching from OC to SC for unpoled and reverse poled conditions. Reprinted with permission.[93] Copyright 2015, American Chemical Society.

5. Impedance and capacitance features of perovskite solar cell devices

So far, the evaluation of time domains during the electrical responses has been reviewed aiming to illustrate how the current and voltage evolve under different conditions. An alternative and very useful method uses a small perturbation signal in the frequency domain. As there are different alternative approaches, we provide a short introduction of impedance spectroscopy, centered on capacitance, and evaluation of similar quantities by the small perturbation time transits.

5.1. Definitions

For convenience, here we first introduce a set of important clarifying concepts as well as experimental set-up descriptions which will be systematically alluded to in the subsequent sections.

Interpretation of measurements and measured quantities. The impedance spectroscopy (IS)[94] analysis has been widely used for the characterization of solar cells.[95] In general, the impedance is the measurement of small perturbation voltage ($\hat{V}$) to current ($\hat{I}$).

In the potentiostatic variant, the IS basically consists of applying an AC potential small perturbation $\hat{V} = V_0 \exp[i\omega t]$ at a given frequency $f = \omega/2\pi$ (using the complex numbers representation where i is the imaginary unit) with respect to the angular frequency ω as in **Figure 10**e. Subsequently, the AC current response $\hat{I} = I_0 \exp\left[i \cdot (\omega \cdot t - \phi)\right]$ of the sample (**Figure 10**f) is detected, ϕ being the phase shift between perturbation and response. The impedance is defined as

$$Z(\omega) = \frac{\hat{V}(\omega)}{\hat{I}(\omega)} \quad \textbf{(3)}$$

The real and imaginary parts of the impedance, Z' and Z'' respectively, are obtained as

$$Z(\omega) = Z' + iZ'' \quad \textbf{(4)}$$

For an ohmic process, the impedance is a constant, $Z = R$, the resistance, that is a positive and real quantity. Under modulation of any system, the kinetic processes produce a frequency dependent response that includes imaginary values.

For the simplest case of an RC circuit, shown in **Figure 10**(a), the complex plane plot representation, $-Z''(Z')$ in **Figure 10**g, exhibits a semicircle. The characteristic time is

$$\tau = \omega_\tau^{-1} = RC \quad (5)$$

with respect to the angular frequency ω_τ that marks the top of the arc. Note that the characteristic resistance R is obtained at zero frequency, $Z(0) = R$. The value $\omega = 0$ in

parenthesis indicates that the displacement is infinitely slow, i.e., $\hat{V}(0)$ and $\hat{J}(0)$ attain a value that is independent of time. For a solar cell with area A, the quotient of the small quantities gives

$$Z(0) = \frac{\hat{V}(0)}{A\,\hat{J}(0)} = \left(A \frac{dJ}{dV} \right)^{-1} = R_{dc} \qquad (6)$$

That is, the small quantities give a derivative of voltage with respect to current. This is the reciprocal of the slope of the $J-V$ curve, which is in turn the dc resistance of the solar cell R_{dc} (per area) in those particular conditions.

In real systems, there is at least a series resistance element that shifts the arc towards the right in **Figure 10**g, and multiple pairs of capacitive and resistive elements can add and/or deform arcs in the complex plane plot. In addition, inductive and/or non-linear elements can also complicate the IS spectra. Concerning the PSCs, a more detailed discussion on the general characteristics of the impedance spectra will be provided in Section 5.5. However, at this point, it is instructive to highlight that no less than two arcs are often presented in the complex plane plots for these devices, at low and high frequency respectively. Therefore, each arc may correspond to an individual mechanism with its own time constant. In this context, several IS studies have reported lifetimes in good agreement with the transient photo-induced measurements,[17] at least with one of the RC constants.

In a discharge experiment in the time domain decay method, we apply a small step of the voltage $\hat{V}(t) = \Delta V \cdot u(t)$, $u(t)$ being $u(t)$the unit step function at $t = 0$, and we observe the consequent evolution of the charge $\hat{Q}(t)$ that passes to the system. However, it is not usually feasible to measure a charge transient, thus we need to observe the current transient $\hat{I}(t)$ and perform an integration:

$$\hat{Q}(t) = \int_0^t \hat{I}(t')dt' \qquad (7)$$

Let us look at this process in the frequency domain. We use the variable $\mathbf{s} = i\omega$, with

$i = \sqrt{-1}$. The Laplace-transformation of a function $f(t)$ to the frequency domain is defined as

$$F(\mathbf{s}) = \int_0^\infty e^{-\mathbf{s}t} f(t)dt \tag{8}$$

Application of the transform to Equation (7) gives

$$\hat{Q}(\mathbf{s}) = \frac{\hat{I}(\mathbf{s})}{\mathbf{s}} . \tag{9}$$

Now we introduce a frequency-dependent capacitance that indicates the modulation of charge with respect to voltage

$$C^*(\omega) = \frac{\hat{Q}(\omega)}{\hat{V}(\omega)} . \tag{10}$$

$C^*(\omega)$ is a function of the frequency, that coincides with the static differential capacitance C at $\omega = 0$, as follows

$$C = \frac{\hat{Q}(0)}{\hat{V}(0)} \tag{11}$$

where

$$C = \frac{dQ}{dV} . \tag{12}$$

We now remark that representing either impedance or capacitance is a matter of choice. Both functions correspond to the same measurement, since they are connected by Equation (9), indeed:

$$C^*(\omega) = \frac{\hat{I}(\omega)}{i\omega\, \hat{V}(\omega)} = \frac{1}{i\omega\, Z(\omega)} \tag{13}$$

or more explicitly

$$C^*(\omega) = -\frac{Z''(\omega) + i\, Z'(\omega)}{\omega\left(Z'(\omega)^2 + Z''(\omega)^2\right)} . \tag{14}$$

However, with respect to graphical presentation, both magnitudes show different information. For a resistive/conductive/recombination process, the arcs in the complex

impedance plane show immediately the different components of resistance, while the capacitance is hidden. On the other hand, a plot of the real part of the capacitance vs. frequency reveals very clearly the charge storage modes of the system that we describe in detail below.

Here, we also note that the usual normalization convention considers capacitance in units of Farads per unit area (e.g. $F \cdot cm^{-2}$). Accordingly, analogous definitions to Equation (10) to (12) should be used, but with the charge expressed in Coulomb per unit area (e.g. $\mathrm{C} \cdot cm^{-2}$). Similarly, impedances and resistances like in Equation (13) to (14) may be presented in Ohms per unit area (e.g. $\Omega \cdot cm^2$).

Physical interpretation of the capacitance. The most basic capacitive response from a solar cell is that of the geometrical capacitance C_g, which only accounts for the sum of the dielectric contribution of each layer between the metallic electrodes. For the typical case of thin film heterostructures, where the classic parallel-plate capacitor is a suitable model, the geometric capacitance per unit area of a device of m different layers in series can be obtained as

$$\left[C_g\right]^{-1} = \sum_m \left[\frac{\varepsilon_0 \varepsilon_{\infty,m}}{d_m}\right]^{-1}, \tag{15}$$

where d_m is the thickness of the m-th layer and $\varepsilon_{\infty,m}$ its relative dielectric constant towards the limit $\omega \to \infty$. Obviously, from Equation (15) it is clear that C_g can be dominated by the layer whose dielectric capacitance is lower in comparison with the rest. Actually, C_g is in general the smaller characteristic capacitance of a sample, thus frequencies above 1 MHz are often needed to determine it.[96]

A second capacitive response to mention is that of the accumulated charge at the edge of the depletion layer in p-n junction-based devices. In the one-side abrupt charge density profile approximation[97], (same as used in Section 3), the depletion layer capacitance per unit area

can be expressed as

$$C_{dl} = \frac{\varepsilon_0 \varepsilon_r}{w} = \sqrt{\frac{q\varepsilon_0 \varepsilon_r N_{eff}}{2\left(V_{bi} - V\right)}}, \tag{16}$$

where q is the elementary charge, w is the space charge width, ε_r and N_{eff} are the relative dielectric constant and the effective concentration of fixed ionized species (approaching N_A or N_D depending the case) respectively of the layer where the depletion zone is placed and V_{bi} is the built-in voltage, also known as flat-band potential. From Equation (16), a few observations can be remarked. First, at equilibrium, $C_{dl} \geq C_g$, since $w \leq d$ for any layer between the metallic electrodes. Therefore, in general C_{dl} dominates the dielectric polarization capacitance in an intermediate frequency range, typically between 1 kHz and 1 MHz. For the latter, C_g shunted by C_{dl} may be considered due to nearly negligible resistive or inductive losses in the bulk and interfaces beyond the space charge, i.e. V between the metallic electrodes matches that between the edges of the depletion region. Second, as reverse bias increase, C_{dl} decreases towards C_g following an inverse square root law $C_{dl} \propto V^{-1/2}$ as the depletion layer is enhanced. In the opposite sense, when the bias is increased towards V_{bi}, C_{dl} grows as the width of the depletion layer is shrunk. And last but not least, the well-known Mott-Schottky (MS) plot is obtained from $C_{dl}^{-2} = 2\left(V_{bi} - V\right)/q\varepsilon_0 \varepsilon_r N_{eff}$ for $V < V_{bi}$ allowing to estimate V_{bi} and N_{eff} from the linear trend.

Notably, the regimen of evaluation for C_g and C_{dl} is that where the displacement currents related with the charging and discharging of the capacitors are around or above the order of the continuous currents through the device. This is the case of low leakage currents (large shunt resistance R_{sh}) and reverse or low forward bias.

In contrast to the reciprocal dependency of dielectric capacitance with the film thickness,

under forward bias around and above V_{bi}, another type of capacitive effect dominates, increasing directly proportional to the film volume. This is due to the bulk charging and discharging during continuous current at a given voltage and it is the chemical capacitance[98] (or diffusion capacitance in older textbooks[97]). This capacitance per unit volume can be normalized with the layer thickness L_μ and hence the capacitance per unit area is given by

$$C_\mu = \frac{q^2 L_\mu N_\mu}{k_B T} \exp\left[\frac{q\,V}{\beta\,k_B T}\right], \tag{17}$$

where k_B is the Boltzmann constant, T the temperature, β a statistic parameter and N_μ is the effective total equilibrium charge density that contributes to C_μ. The nature of N_μ, for instance, can be related with minority holes/electrons or traps, depending on the case. Note that Equation (17) describes C_μ for systems where the use of the Boltzmann statistics is reasonable, however, for other systems, it can be approximated by $C_\mu = q^2 L_\mu \cdot dN/dE$,with dN/dE being the total density of states.[44]

Capacitance from small perturbation transient methods. A capacitance measurement is also acquirable from the transient responses to small light perturbations, like in the case of the photoinduced differential charging (PI-DC).[83, 84] In this case, PI-TPC and PI-TPV are performed under the same light pulse, at SC and OC respectively, as introduced in Section 4.1. From PI-TPC, the extracted charge per unit area is obtained by calculating the integral of the current density, which results in $\Delta Q = \Delta J_{sc}\tau_{sc}$ in the case of a monoexponential current decay $\Delta J_{sc}\exp\left[-t/\tau_{sc}\right]$. Subsequently, from PI-TPV, the amplitude ΔV_{oc} is taken and then Equation (12) is approximated to

$$C = \frac{\Delta Q_{sc}}{\Delta V_{oc}} = \frac{\Delta J_{sc}\tau_{sc}}{\Delta V_{oc}}. \tag{18}$$

Here, two assumptions should be considered: (i) the charge losses at SC in the solar cell under illumination are negligible and (ii) the solar cell photocurrent value is linear with the

increase of sun-simulated light intensity and bias independent. Also note that the measurements of ΔV_{sc} and ΔV_{oc} in (18) are made under different operation conditions, SC and OC respectively, thus implying different resistances. Therefore, it is commonly found that capacitance from PI-DC differs in amount from that of IS.

Regarding the characteristic time τ_{sc}, it should not be mistaken with other magnitudes (e.g. recombination lifetime) given that it may account for the charge extraction processes, which are expected to depend on the resistive features of the sample (e.g. bulk, contacts, interfaces). It is also expected that τ_{sc} will be a faster time than that required for the recombination at OC. However, it is often found that non- or multi-exponential J_{sc} decays occur, which makes the interpretation of these transient responses difficult, e.g. due to the competition between majority and minority carriers processes or in more challenging systems like PSCs.

More importantly, the chemical capacitance character of C in Equation (18) must be ensured given that PI-DC is habitually performed at forward bias, i.e. with different intensities of background illumination. If not, and without clarifying considerations of such capacitive nature, the ratio of Equation (18) could be reporting on phenomena different from that of the rearrangement of charges due to the change in the chemical potentials of the carriers.

As well, from the PI-CE,[83, 84] also introduced in Section 4.1, different V_{oc} values can be estimated by changing the light intensity and the corresponding charge can be integrated after switching from OC to SC. Thus, the capacitance behavior with V_{oc} can be obtained as

$$C = \frac{dQ_{sc}}{dV_{oc}} = \frac{d\left(\int J_{sc} dt\right)}{dV_{oc}} \quad . \tag{19}$$

However, care should be taken with the interpretation of this charge extraction PI-CE capacitance, since the charge extracted from the decay does not account for a small perturbation process, unlike the IS and PI-DC methods.

Capacitance in voltage sweep. For the evaluation of capacitive responses, apart from IS and photo-induced transient measurements, cyclic voltammetry (CV) is often employed. CV

basically consists of the continuous bias sweep from an initial voltage V_0 to a different V_1 and then back to V_0 at a given scan rate $s = dV/dt$, whose sign depends on the direction of sweeping. In contrast to Equation (10) that defines the small amplitude measurement, the CV and related voltage sweep techniques produce a continuous measurement and large amplitude response signal.

If we assume that the measured current is capacitive, then the current is calculated as

$$J_{cap} = \frac{dQ}{dt} = C\frac{dV}{dt} = s\ C \tag{20}$$

and the capacitance can be obtained as $C = J_{cap}/s$ from the measured current.

5.2. Dark capacitance and dielectric components

By using IS, the capacitance spectra of PSCs can be obtained as in **Figure 15**. In dark equilibrium, two main plateaus can be identified in the Capacitance-frequency plot at frequencies below those where the series resistive and inductive effects are present. Accordingly, at least two characteristic capacitances should be identified with their respective characteristic resistances and hence, two arcs are expected from the complex plane plot, as in the inset of **Figure 15**. This general trend is not exclusive of solar cell structures, taking into account that symmetrically contacted bulk perovskite layers can deliver the same features.[64]

Regarding the high frequency (**Figure 15**) behavior, a dielectric polarization of domains takes place, whose corresponding capacitance approaches C_g. Guerrero and co-workers[64, 99] corroborated this plateau to fulfill Equation (15) at room temperature and reported dielectric constant values around 22-24 for $MAPbI_3$. The latter was in good agreement with previous calculations (23.3) of Onoda-Yamamuro et al.[100], who fitted the Kirkwood-Fröhlich equation and also agreed with predictions (24.1) of Brivio et al.[101] from DFT simulations with quasi-particle corrections.

Importantly, several phase transitions occur even in the operational temperature range, e.g.

$MAPbI_3$ changes from orthorhombic to tetragonal structure around ~150 K (space applications) and from tetragonal to cubic around ~57°C, which produce gaps in the dielectric constant. The latter is illustrated in the literature,[13, 27, 28, 100, 102, 103] as well as the complete dark capacitance spectra below[13] and above[104] room temperature.

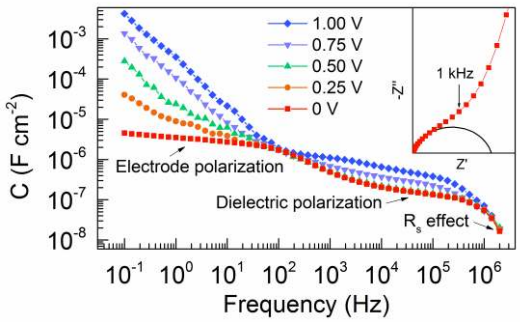

Figure 15. Capacitance-frequency plot of dark capacitance spectra from IS of a $MAPbI_3$-based cell at different forward bias, as indicated. Here, the low frequency capacitance is enlarged due to injected charge effects. Inset: the corresponding complex plane plot. Reprinted with permission.[105] Copyright 2016, AIP Publishing.

Another important effect on the dark high frequency capacitance is that of applied voltage, which critically depends on the bias range and device charge density. At reverse bias, the capacitance often saturates towards C_g, as illustrated in **Figure 16**, meaning full depletion of the space charge zone. However, care must be taken when interpreting the capacitance in the Mott-Schottky plot representation at forward bias because at least two different capacitances compete below and around V_{bi}. Like in the experimental data in **Figure 16**a, some devices actually present a nearly constant charge density profile $\rho(x) = qN_{eff}$ (negative if $N_{eff} \approx N_A$), x being the distance from the junction. Hence, the Mott-Schottky analysis is meaningful and the fitting of the linear region of low forward bias gives N_{eff} and V_{bi}. However, in most cases, the quasi intrinsic character of the perovskite and variable doping by vacancy displacement prevents the use of this technique, which is the situation of **Figure 16**b. For such samples, the

fitting of the nearly linear region around equilibrium (**Figure 16**b dashed red line) would deliver a meaningless V_{bi} value, and the fitting of the apparently linear abrupt step around the expected V_{bi} (**Figure 16**b solid red line) is the transition to a dominant exponential capacitance that appears as flat band potential is approached and exceeded (see **Figure 16** right axes). Consequently, Mott-Schottky analysis is not useful here. Actually, for some devices, the shape of the charge density can be approximated to a power law $\rho(x) = q\eta x^{\gamma}$ (η, a constant with units of $\mathrm{cm}^{-(\gamma+3)}$ and γ, an integer). Thus, by integrating the Poisson equation (analogously to Section 1.1 in Supporting Information) along a depletion layer of width *w*, it is easy to obtain after some calculations[97, 106]

$$C_{dl}{}^{-(\gamma+2)} \propto \frac{(V_{bi} - V)}{\eta}. \tag{21}$$

For instance, the capacitance of **Figure 16**b gives a clear linear trend around equilibrium when represented as $C^{-16}(V)$ in **Figure 16**c. This suggest that a depletion layer capacitance from a charge density profile like $\rho(x) = q\eta x^{14}$ can dominate the capacitive response if $V_{bi} \approx 1\ \mathrm{V}$. Note that this assumption is considered as a correction of N_A (assuming p-type perovskite) in Equation S8 of Section 1.1 in Supporting Information, thus it cannot be mistaken as an effect of mobile ions like Equation S15 in Section 1.2.1 in Supporting Information.

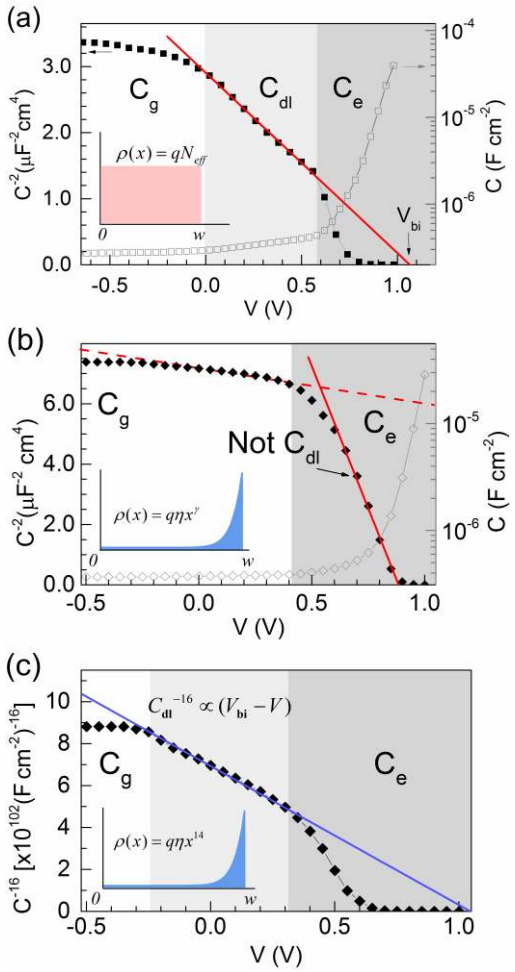

Figure 16. Mott-Schottky plots (left axes) and corresponding capacitance-voltage curves (right axes) at 10 kHz for two devices of different perovskite: (a) with and (b) without constant charge density profile. In (c), the capacitance of (b) as C^{-16}(V) is presented, thus a 14th power law charge density profile results in a more suitable condition when assumed $V_{bi} \approx 1$ V. Inset in each graph is the respective absolute charge density. Adapted with permission.[105] Copyright 2016, AIP Publishing.

Additionally, once the DC current becomes substantial, at high enough forward bias, an exponential capacitance C_e arises as in **Figure 16**, right axes. This can be also roughly appreciated from **Figure 15** between 0.5 V and 0.75 V around few tens of kHz. Regarding the nature of this C_e, a chemical component (Equation (17)) could be expected, however, an overlapping occurs with slow mechanisms that presumably rules the low-frequency

capacitance (C_s). The effect of the sluggish processes on high-frequency capacitance can be straightforwardly appreciated from capacitance-voltage curvesat different scan rates and directions showing a hysteresis similar to that of *J-V* curves.[105, 107] Contrasting the argument on **Figure 16**c, this effect could be related to the features discussed earlier in relation with mobile ion distributions which are introduced in the Poisson equation (see **Equation S15)** in Section 1.2.1 in the Supporting Information. In addition, for inverted cells with organic selective contacts, where nearly negligible hysteresis is obtained from *J-V* curves, (see Section 6.6), faradaic current peaks can affect the $C(V)$ measurements even at frequencies as high as 10 kHz.[107] The dc polarization may be responsible for the drift of ions toward the interphases where the charge accumulation could be a catalytic factor for reactivity in a reversible or irreversible way (degradation), as shown in **Figure 1**f.

Importantly, calculations by Garcia-Belmonte and coworkers[108] have shown C_μ of $MAPbI_3$ to be far below C_g. This was done considering (i) the $MAPbI_3$ low intrinsic density of defects (~10^5 cm^{-3}, similar to CdTe but 5 orders below Silicon) and (ii) the condition when generated carriers exceed majority carriers around 1 V forward bias ($\beta = 2$ in Equation (17)). Consequently, in practice, it would not be possible to measure C_μ, unless (i) larger intrinsic density of states actually occurs or (ii) minority carriers do not surpass majorities at 1 V ($\beta \to 1$ in Equation (17)).

Last but not least, at low frequency, there is a remarkable enlargement of the capacitance which is exponentially magnified as the electronic charge is injected (**Figure 15**) or generated (see **Figure 19**). In this regime, there is no clear distinction between forward bias below or above the flat band potential and the capacitance systematically grows. This can be seen in the Capacitance-frequency plot of **Figure 15** around a few fractions of Hz, while in the complex plane representation (inset of **Figure 15**), it results in a deviation from the high frequency arc whose extrapolation can show resistances up to MΩ. Notably, experiments by Almora et al.[13] on cells with different thicknesses in perovskite layers showed no clear correlation between

$MAPbI_{3-x}Cl_3$ thickness and the low frequency capacitance, so they proposed that electrode polarization and surface processes should be behind this effect. In addition, they calculated a characteristic dark capacitance by subtracting the J_{cap} from the current density-voltage curves at different scan rates, as in Equation (21), whose results are illustrated in **Figure 17**, showing magnitudes in the range of $\mu F \cdot cm^{-2}$. Moreover, despite the dark J_{cap} being less than $\mu A \cdot cm^{-2}$, below flat band condition, they grow exponentially as carrier injection rises and reach larger than $mA \cdot cm^{-2}$ values under light, irrespective of the bias regime.

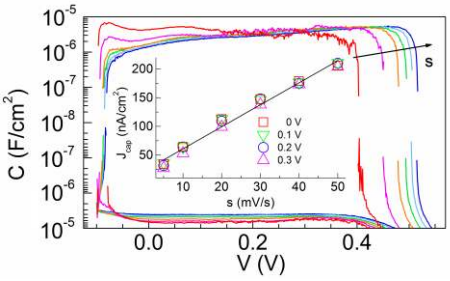

Figure 17. Capacitance from dark *J-V* curves at different scan rates of a $MAPbI_{3-x}Cl_x$ based PSC, as indicated. Inset: Capacitive current versus scan rate at different forward bias values, yielding a capacitance of 3.8 $\mu F \cdot cm^{-2}$ from the linear fit. Adapted with permission.[13] Copyright 2015, American Chemical Society.

5.3. Capacitance from light-induced transients

Figure 18 illustrates some typical results for PI-CE and differential charging PI-DC for PSCs, which in general reproduce an exponential trend as approaching V_{bi} like in **Figure 16**. As introduced in Section 4.1, differently to other cell types, the transient decays from PI-TPV, PI-TPC and PI-CE present at least two characteristic times during relaxations. This was interpreted by O'Regan et al.[86] as evidence of multiple mechanisms of charge storage within the cell. Additionally, they point out that for PSCs, the capacitance from PI-DC results are significantly lesser than that from PI-CE, as a consequence of the differences in the current

relaxation time scales. This has been subsequently checked by Palomares and co-workers in several studies,[87, 88, 109, 110] in which they also realized a crucial effect due to the composition and morphology of the selective contacts.

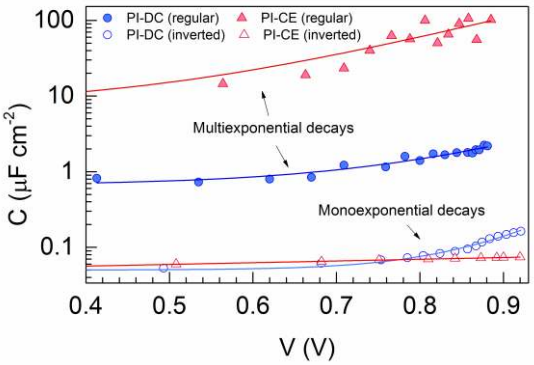

Figure 18. Capacitance as function of V_{oc} from PI-DC (circles) and PI-CE (triangles) for two devices: TiO_2/$MAPbI_3$/spiro-OMeTAD (filled dots) and PEDOT/$MAPbI_3$/PCBM (open dots). A clear difference between techniques arises when multiexponential decays occur. Data courtesy of Emilio Palomares.

A slower charge extraction at SC in PI-CE than charge recombination at OC in PI-TPV is meaningless without considering the influence of extra phenomena. The core of the discussion here lies on the doubts regarding the chemical nature of the capacitance measured by these means. For example, feasibly during the PI-CE charging at 1 sun illumination, besides charge accumulation as C_μ, surface polarization at the electrodes create extra concentration of charge whose ulterior relaxation time is considerably slower. This is a big ionic–electronic accumulation effect, whose occurrence has been concluded several times in the literature[2, 55] and it is explained here by simulations in Fig. 3 and S2. Contrarily, for PI-DC, a steady state is secured prior to the small perturbation, that is possibly too fast for the slow mechanisms. All of these can be related with the above (see also next sections) mentioned low frequency capacitance: in other organic solar cells and dye sensitized solar cells (where there is no C_s),

the capacitances from PI-CE and PI-DC coincide. Actually, a recent work[111] showed comparable charge carrier densities both from PI-CE and PI-DC on $MAPbI_3$–based cells with organic selective contacts, also known as inverted configuration. These devices have been shown to have significantly lower C_s in comparison with those that typically include TiO_2 and spiro-OMeTAD as selective contacts.[57, 107] **Figure 18** shows the clear difference between PI-CE and PI-DC for devices with multiexponential decays (typically those with $TiO_2/MAPbI_3$ interface) while for monoexponential decays, both techniques deliver not so distinct values. Among cells with monoexponential decays, those with organic selective contacts are a good example, despite some optimized regular devices also showing this feature.

5.4. The low-frequency capacitance under steady state illumination

The appearance of an anomalously large C_s under illumination is one of the clearest evidences of the presence of slow dynamic charge mechanisms in PSCs. This feature has been reported by several research groups[7, 55, 56, 112-114] mainly with the aim of illustrating its dependence with the composition and morphology of the selective contacts as well as the close relation with the widely discussed hysteresis behavior in the $J-V$ curves (see Section 6).

As shown in **Figure 19**, the general trend of the spectra is not so different from that created by charge injection throughout forward bias at dark (**Figure 15**), meaning that the explanation behind such an effect is directly related with the increase of electronic charge density either by injection or photogeneration. As summarized by Bisquert et al.,[109] explanatory proposals include (i) change of electrode polarization,[13] (ii) change of bulk polarizability,[115] or (iii) change of chemical capacitance.[104]

The first argument, where ionic species pile up at the interface, can explain equilibrium dark C_s in the order of $\mu F \cdot cm^{-2}$. This situation of dipolar distribution of ions towards the

anode and the cathode has already been presented in Section 3.3 with related profiles and band-diagrams. Almora et al.[64] found evidence that shows a combination of Helmholtz capacitance C_{HL} and diffusion layer capacitance

$$C_{diff} = \frac{\varepsilon_r \varepsilon_0}{L_D} \cosh\left[\frac{qV}{2k_B T}\right] \tag{22}$$

in a Debye length as in Equation (1) for conditions where $C_{HL} \sim C_{diff}$. Note that these capacitances are connected serially, thus the nearly constant C_{HL} prevents the total capacitance to achieve values larger than tens of μF·cm^{-2}, thus the enhancement of C_s under larger charge densities cannot be explained in terms of C_{diff} increase due to the series configuration.

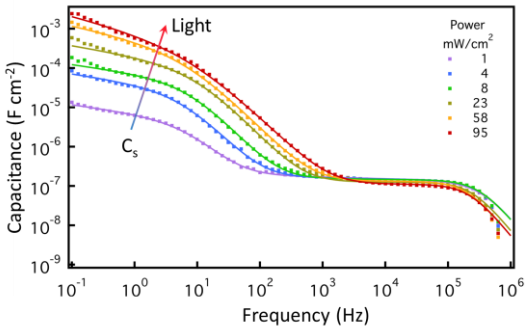

Figure 19. Capacitance spectra of a $MAPbI_3$-based PSC at SC for different illuminations as indicated. Here, the low frequency capacitance is enlarged due to generated charge effects. Adapted with permission.[114] Copyright 2016, American Chemical Society.

Therefore, C_{HL} should no longer be significant under light or forward bias in order to achieve capacitances as large as mF·cm^{-2}. This can happen as a consequence of a large concentration of carriers form a large interfacial capacitance.[115] Similarly, it is possible that there are C_μ effects, however, an important role from native defects could also be expected, as suggested by Li et al.[112]

Following the idea of a large surface capacitance due to accumulation of electronic carriers,

the works by Zarazua et al.[55, 114] showed a clear experimental $C_s \propto \exp[qV/2k_BT]$ dependency. This will be a consequence of a band bending induced by light that is contrary to the equilibrium Schottky barrier, with the majority carriers entering an accumulation regime. Assuming a p-type semiconductor at the $MAPbI_3$-TiO_2 interface, the accumulation capacitance has the expression

$$C_s = \sqrt{\frac{p_b}{2}\frac{q^2\varepsilon_r\varepsilon_0}{k_BT}}\exp\left[\frac{qV}{2k_BT}\right], \tag{23}$$

where p_b is the bulk carrier density corresponding to native defects. Interestingly, Equation (23) resembles the exponentially growing term of C_{diff} from Equation (22), but considering $N = 2p_b$ in Equation (1). This could mean that the general mechanism is not so different in nature; hence, strongly linked ionic-electronic features possibly govern the slow processes. However, in contrast to the ions being blocked at the interface, the electronic accumulation does not find a series limitation and can rise to very high values. For instance, the experiments with the perovskite thickness d are illustrative of the regimens where each charge type is of most importance. In dark equilibrium, C_s is almost d independent or nearly inversely proportional,[13] while upon increasing electronic charge density, C_s grows proportionally with d [113, 114] indicating the dependence of surface capacitance on charge collection length. Importantly, the linear behavior $C_s \propto d^{-1}$ in the dark has not been clearly obtained, which discards the idea of its origin as purely bulk dielectric in nature. Although in most cases $C_s \propto d$ in light/forward bias, the bulk chemical capacitance mechanisms can be ruled out.

5.5. Negative capacitance and the equivalent circuit

As commented above in Section 5.2 with respect to **Figure 15**, the most typical impedance response from PSCs may include two capacitances with their respective resistances that generate two arcs in the complex plane representation of impedance and two plateaus in the

capacitance-frequency representation of capacitance. Subsequent discussion stated the nature of the low frequency region as corresponding to slow mechanisms possibly associated with ionic/electronic interface processes (C_s, R_s), while the high frequency branch of spectra are in principle related with dielectric bulk polarization (C_{bulk}, R_{bulk}). Additionally, further phenomena can also occur, generating intermediate arcs/plateaus in the IS spectra. However, in some cases, even inductive loops can be found in the impedance plots whose corresponding capacitances result in negative values, as reported initially by Sanchez et al..[17]

Special attention to these patterns was paid by Guerrero et al.[99], who studied the IS spectra from diverse configurations. For example, **Figure 20**a illustrates the loops in the Complex plane plots for different ESL thicknesses, showing a critical dependency. Particularly for the loop in the middle (15 nm ESL), a portion of the spectrum lies below the level of zero imaginary impedance ($Z'' > 0$) which implies a negative capacitance, like in **Figure 20**b.

A proper model for the IS response is provided by the equivalent circuit of **Figure 20**c, which successfully reproduces the experimental patterns as indicated by the solid lines in **Figure 20**a,b. In addition to the series resistance R_{series}, the low frequency circuit (C_s, R_s) is set in series with the high frequency resistance R_{bulk} and all of these are shunted by the high frequency capacitance C_{bulk}. Notably, in this configuration, R_{bulk} accounts for bulk resistive contributions, and possibly also contact related impedance, in regions different from that of the voltage drop associated with R_s; e.g. if R_s corresponds to a L_D region towards the ESL contact, R_{bulk} would include remaining resistive effects within the device. By only using these five elements (R_{series}, C_{bulk}, R_{bulk}, C_s, R_s), most of the IS spectra can be effectively modeled towards the high and low frequency limits in PSCs.[114] This configuration (without the elements in red of **Figure 20**) is also known as Matryoshka equivalent circuit.

Nevertheless, sometimes there is a need for the inclusion of a third pair C_3 and R_3 in series with the low frequency components (C_s, R_s), that often modifies the transition between the

two arcs/plateaus. For instance, in the complex plane plot, the characteristic intermediate frequency $f_3 = \left(C_3 \cdot R_3\right)^{-1}$ will determine if a distortion is apparent on the high frequency arc or towards low frequencies. For the capacitance spectra of **Figure 20**b, f_3 is in the order of hundreds of Hz which modifies the transition between C_{bulk} and C_s, that seems to be ESL thickness independent. In addition, the appearance of loops can be understood as the effect of an inductive element $\boldsymbol{L}$ shunting C_3 and R_3. These three elements are highlighted (red) in the equivalent circuit of **Figure 20**c, although they are not always present or not measurable in practice. The physical meaning of C_3, R_3 and $\boldsymbol{L}$ can be related with both bulk and contact processes and they take place in poor performing devices as well as in cells with high PCE. Specifically, C_3 has been suggested to be associated with an additional electronic surface state that has a large impact on recombination.

Recently, an interesting demonstration was recently made by Fabregat-Santiago et al.[116] who correlated the observation of this negative capacitance directly with a corresponding decrease in performance of a halide perovskite (HaP; $CsPbBr_3$)-based devices, expressed as reduction of V_{oc} and FF. Furthermore, they employed some variants of the equivalent circuit of **Figure 20**c and, with the dc approximation, were able to reconstruct the $J-V$ curves from the IS spectra of cells with and without negative capacitance.

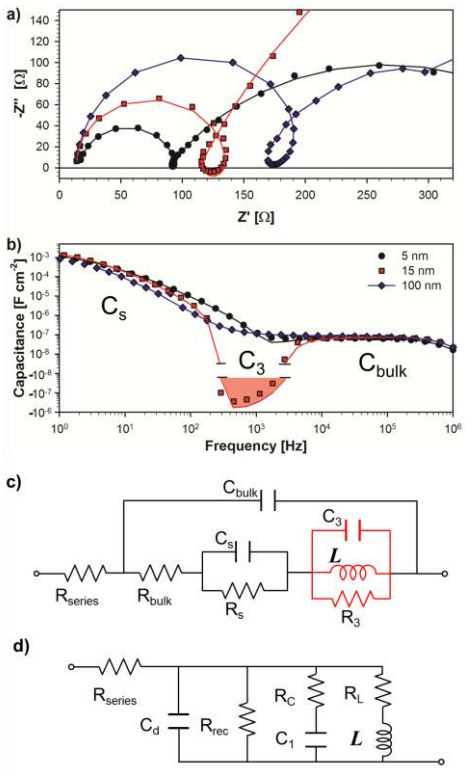

Figure 20. IS spectra for $FA_{0.85}MA_{0.15}Pb(I_{0.85}Br_{0.15})_3$-based cells with different thicknesses of SnO_2 ESL, as indicated. Impedance Complex plane plots in (a) and corresponding Capacitance-frequency plots in (b). The measurements were carried out at SC under 1 sun light intensity. The solid lines represent the fittings to equivalent circuit in scheme (c), a general model for PSCs. Highlighted in red is the sub-circuit of elements C_3, R_3 and $\boldsymbol{L}$, whose effects are not always measurable in practice. Adapted with permission.[99] Copyright 2016, American Chemical Society. (d) Alternative equivalent circuit as proposed by Bisquert and co-workers.[117]

Remarkably, in a subsequent work[117], a family of theoretical IS spectrum patterns with the inclusion of inductive loops was provided based on a previously developed surface polarization model[2] (see Section 6.4). In that study, an approach different from that of the equivalent circuit of **Figure 20**c was proposed, with the advantageous direct identification of recombination resistance R_{rec} and surface charging capacitance C_1. This equivalent circuit is observable in **Figure 20**d, where C_d is the dielectric capacitance and R_L is the series

resistance with $\boldsymbol{L}$. In addition, a characteristic relaxation kinetic constant was straightforwardly associated with the inductive element $\boldsymbol{L}$. Also, Anta and co-workers[118] summarized on further possible alternatives of equivalent circuits. Furthermore, they provided a handy methodology for avoiding mistaken processing of IS measurements.

6. Current-voltage curve hysteresis

The phenomenon of hysteresis in perovskite solar cells has been plaguing the scientific community for several years now. It has been known that perovskite solar cells are highly sensitive to several experimental parameters such as pre-biasing voltage and time, scan rate and light intensity.[1, 15] This promotes large anomalies in the current-voltage curve of the cell and prevents obtaining a stabilized output power at a given point in the curve. The origin of the hysteretic effects in the perovskite solar cell is quite strongly correlated with the slow timescale phenomena observed from transient experiments such as open-circuit voltage decays[8, 17, 89] and IS measurements[7, 13] (see Section 4 and 5), due to the simple fact that the slow timescale phenomena in the order of a few seconds is comparable to the scan rate in a standard *J-V* measurement. This effect is representative of the majority of the PSCs reported in literature (even in cases where not noticed or virtually neglected) and therefore, an adequate resolution of the problem of dynamic hysteresis remains a very important and relevant question that needs to be solved.

We formally define the distortions in current-voltage characteristics based on specific measurement protocols as dynamic hysteresis (hereafter alternatively referred to as hysteresis). For convenience, we also define the scan from the starting forward (F) voltage to the final reverse (R) voltage as the FR scan, and vice versa as the RF scan. While a number of different types of dynamic hysteresis have been reported in the literature, in the work by Ravishankar et al.[2], a summary of the general observed features was shown as in **Figure 21** whose description is listed as follows:

(a) Capacitive hysteresis – This typically shows a symmetric current above and below the apparent steady state photocurrent value depending on the direction of the voltage scan in a manner identical to a capacitive discharge.[17, 93, 119] This capacitive current increases linearly with the scan rate (inset **Figure 17**) and has been observed in dark measurements as well (**Figure 22**a).[13]

(b) 'Bump' close to V_{oc} – When the scan goes from F to R, there occurs a maximum in the current close to V_{oc} which is actually larger than the short-circuit photocurrent. This behavior has a strong dependence on the applied bias before the scan.[15, 120, 121]

(c) Apparent photocurrent enhancement in FR direction – This behavior is usually observed at large scan rates, where the photocurrent value is enhanced compared to the steady state case while the V_{oc} and forward bias resistance are unaltered.[5, 15, 121-123]

(d) Strong decay of photocurrent in RF direction – This phenomenon is highly dependent on the scan routine and is also accentuated at large reverse pre-bias values.[5, 19, 124]

(e) Apparent V_{oc} shift for RF scan – This behavior is the most commonly observed for perovskite solar cells where the RF scan delivers a reduced V_{oc} compared to the FR scan.[119, 124-126] J_{sc} and low forward bias resistance are not modified. Subsequently, a mismatch between the initial and final current after a loop may occur.[107] The combination of **Figure 21**d and **Figure 21**e patterns is generally referred to as 'normal hysteresis'.

(f) Inverted hysteresis – Here, the RF curve exceeds the FR within some region between short-circuit and open-circuit,[125, 126] unlike all previous patterns where the absolute current is always lower in RF direction than in FR. For less efficient cells, the crossing is accentuated and can occur at low forward or even reverse bias. [127] This phenomenon is sensitive to initial bias before the scan[126] and will be more widely discussed in Section 6.5.

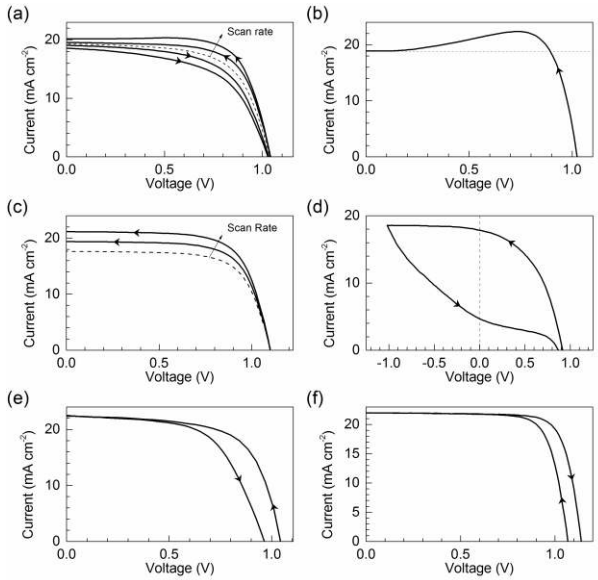

Figure 21. Summary of dynamic hysteresis trends in perovskite solar cells. The arrows show the direction of the sweep. Dashed lines indicate the steady state curve in (a,c), J_{sc} and zero bias in (b) and (d) respectively. Adapted with permission.[2] Copyright 2017, American Chemical Society.

It must be noted that the majority of the diverse hysteretic trends shown in **Figure 21** involve strong variations in the photocurrent, which is symptomatic of low efficiency perovskite solar cells. For high quality, state-of-the-art perovskite solar cells, the photocurrent values are very stable and the dominant factor governing the type of hysteresis is variations in V_{oc}, akin to **Figure 21**f. The rapid improvement in the quality of the perovskite layer in labs all over the world will eliminate any transport limitations in the perovskite, leading to hysteresis that is dependent only on contact properties and/or specific recombination mechanisms at a given state of the solar cell. This distinction will have a significant impact on the modeling of high efficiency perovskite solar cells, which is tackled in subsequent sections.

6.1. Dark *J-V* curve hysteresis

O'Regan et al.[86] showed early on that hysteresis is not necessarily a light driven process from their studies of dark current evolution under bias. Dark hysteresis in PSCs has been

broadly reported in the literature,[13, 25, 43, 107, 126, 128] in general signifying that similar to **Figure 21**, dark patterns can be obtained, only that under illumination, the effect is enhanced by the augmentation of generated electronic charge density.

Particularly, several works by Almora and co-workers[13, 43, 107, 128] have illustrated dark hysteresis in the useful representation of logarithm-scaled currents, as in **Figure 22**. In these works, constant capacitance-related current J_{cap} at different scan rates, like Equation (20) were added to typical diode curves resulting in apparent J_{sc} and V_{oc} values for faster bias sweeps. Note that the log vertical scale increases for either positive or negative currents, to show clearly the opening of capacitive currents. Typical experimental capacitance extracted from **Figure 22** behavior can be found in **Figure 17**, which is responsible for the apparent yielded power when performing FR bias sweep. In this representation, it is also easy to see non-capacitive current effects when the scan rate is slow enough; this is a subject discussed in Section 6.5.

The representation of **Figure 22**a can serve as a comparison tool among samples with different hysteresis degrees. This is due to the advantage of measuring in a less stressful configuration (dark), so effects like degradation are fewer. Furthermore, it could be thought that the commonly used empirical hysteresis index[17, 128] does not have validity in dark. This quite intuitive parameter is defined as

$$HI = 1 - \frac{J_{RF}(V_{hyst})}{J_{FR}(V_{hyst})}, \tag{24}$$

where J_{RF} and J_{FR} are the currents at RF and FR scan directions, respectively, and V_{hyst} is a convenient bias (e.g. $V_{hyst} = V_{oc}/2$,[17] $V_{hyst} = 4V_{oc}/5$),[113] resulting in $\mathrm{HI} \to 1$ when more hysteresis and $\mathrm{HI} \to 0$ when less. However, it is precisely within the bias range between 0.5 V and 0.6 V (approximately $V_{oc}/2$ at 1 sun) where the dark hysteretic currents are more prominent, as evident from **Figure 17**, **Figure 22**a and clearly in **Figure 22**b. Actually, HI can straightforwardly account for the presence of normal hysteresis (HI<1) or even inverted

(HI<0) at a given voltage. The latter graphic advantage can be appreciated in a recent work[129] on tunable hysteretic features (see Section 6.5) where an analogue parameterization to Equation (15) was used.

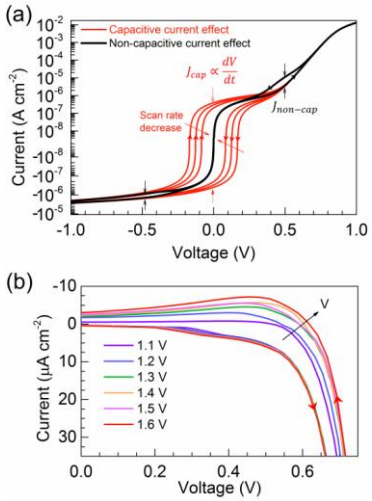

Figure 22. Dark *J-V* curves hysteresis. (a) Simulation of capacitive and non-capacitive hysteretic effects at different scan rates with logarithm scaled currents. Adapted with permission.[107] Copyright 2016, American Chemical Society. (b) Experimental $J-V$ curves of a $MAPbI_3$-based device at 100 $mV \cdot s^{-1}$ for different initial biases, as indicated. Reprinted with permission.[2] Copyright 2017, American Chemical Society.

Interestingly, as presented in **Figure 21**b, the origins of this characteristic current maximum above the corresponding J_{sc}, or bump, has been argued to be due to either capacitive currents or to changed quasi-steady state photocurrent generation.[5] The first explanation is related to the discussion on C_s from Section 5 and its effect on the *J-V* curve. About this, **Figure 23** in Section 6.2 illustrates that these capacitive currents can be as high as $5\ mA \cdot cm^{-2}$, thus the needed asymmetry for the bump of **Figure 21**b pattern should be an effect of a given preconditioning. On the other hand, from the second possibility, it would be expected that the current maximum (bump) will never exceed the actual or steady state J_{sc}

since only modifications in the recombination and/or charge extraction are considered. In any case, a combination or overlapping of both effects could be happening, but it should be noticed that *J-V* curves in **Figure 22**b expose the same bump pattern in dark (where $J_{sc} = 0$). Despite capacitive currents in **Figure 22**b being within the order of $\mu A \cdot cm^{-2}$, the asymmetric formation of the capacitive dark bump favors the explanatory hypothesis of charge accumulation mechanisms upon prior biasing. Nevertheless, extra confirmation is still lacking since no bump has been reported for devices with J_{sc} close to the theoretical photocurrent limit (around $22\ mA \cdot cm^{-2}$ for a 200 nm thick $MAPbI_3$ layer).[33]

6.2. Capacitive hysteresis and step voltage scans under illumination

The analysis of $J-V$ curves, while useful, do not easily provide in-depth information regarding transport, recombination and capacitive properties of the device. Instead of the scan rate, a better metric would be using a delay time between consecutive voltage steps, which shows the timescale of recovery of the current to a new steady state upon a voltage step.

The use of large voltage steps compared to the values used in standard *J-V* measurements allows the visualization of the timescale of the slow transients quite clearly. We refer to such measurements as step voltage scans or step scans. The step scans are generally reported with photocurrent as a function of time or by plotting the photocurrent at the end of each delay time sequence versus applied voltage.

Figure 8a shows the general trends observed for step scans on PSCs.[15, 93, 113, 130] The photocurrent transients are seen to change direction depending upon the sign of the applied voltage step, where in the case of the FR scan, upon stepping the voltage to a lower forward bias value, a sharp increase in the photocurrent occurs followed by a slow decay to the steady state value. This trend is reversed in the RF scan, where there is a sharp transient photocurrent in the direction of recombination followed by a slow increase in current until it reaches steady state. For the FR scan, the magnitude of the non-steady state photocurrents show a strong

dependence on the applied bias with a maximum close to V_{oc} followed by a drop-off in either direction. The decay lifetimes of these non-steady state photocurrents were observed to be in the range of a few hundred milliseconds to a few seconds.[15, 93, 120]

The trends of the photocurrent plotted versus voltage for step scans are shown in **Figure 23**b and **Figure 23**c. For the FR scan, the short-circuit photocurrent value increases for shorter delay times, similar to the case of **Figure 21**c. In certain cases, as in **Figure 23**b, a 'bump' is observed close to V_{oc}, similar to **Figure 21**b. The shape of the FR scan can also take the shape of **Figure 21**e, as seen in **Figure 23**c. In general, the V_{oc} for FR scans at different delay times is the same or slightly increases for shorter delay times. For the RF scans, the V_{oc} consistently reduces for shorter delay times.

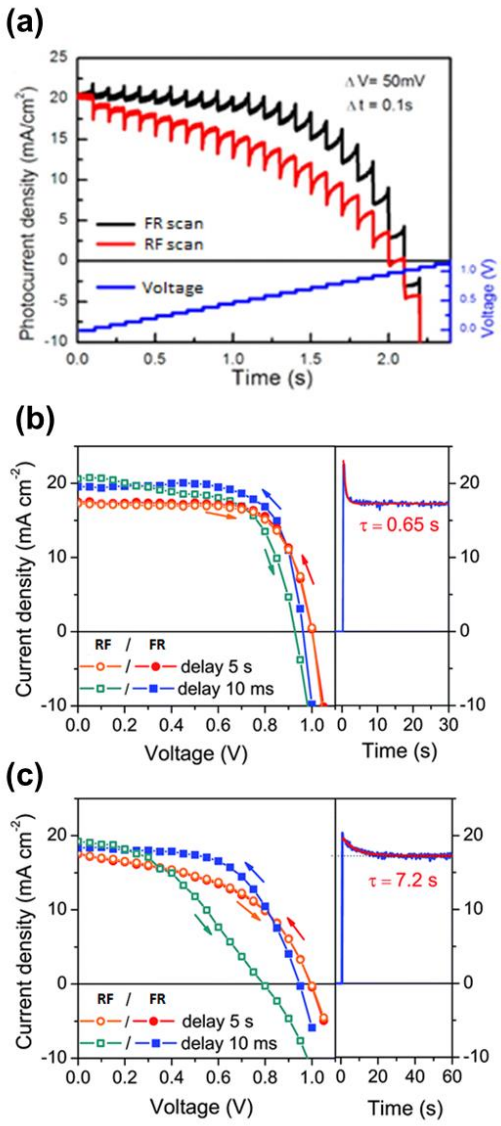

Figure 23. (a) Evolution of current versus time for step voltage scans in the FR and RF directions (Forward to reverse (FR) and reverse to forward (RF) bias). Voltage step size and delay time shown in inset. Reprinted with permission.[93] Copyright 2015, American Chemical Society. Stepped voltage scan curves for (b) $MAPbI_3$ solar cell with mesoporous TiO_2 scaffold and (c) solution processed planar $MAPbI_3$ solar cell for different delay times as shown in the bottom. Inset on the right of (b) and (c) show the respective photocurrent decays versus time when switching from open-circuit to short-circuit conditions. (b) and (c) reprinted with permission.[15] Copyright 2014, Royal Society of Chemistry.

However, there exists a variability in the trends of the short-circuit current values for the RF scan, wherein it increases for shorter delay times,[15] as seen from **Figure 23**b and **Figure 23**c, while others[113, 120] have observed that the short-circuit current decreases for shorter delay times. While a consistent interpretation unifying the observed trends has not been achieved, several broad mechanisms have been correlated with the trends of the step voltage scans. The capacitive discharge upon voltage stepping has been attributed to electronic and/or ionic accumulation at the contacts,[93] or ferroelectric depolarization,[15] correlated to the large low frequency capacitance observed from IS.[93] The slow component following the capacitive discharge is interpreted as arising from the slow migration of ions through the device,[15, 93] which can modify the efficacy of extraction of photogenerated carriers or from the reorientation of ferroelectric domains in the device.[120]

6.3. Effect of pre-conditioning on *J-V* curves

From Section 4, it has been clear that the transient evolution of PSCs is critically dependent on the history of the sample. For instance, **Figure 14** showed effects of different prior biasing on current while **Figure 13** summarized on studies on voltage decays after light or dark conditions. Evidently, these effects are also appreciable when performing $J-V$ curves.

Voltage preconditioning has a significant impact on the FF and PCE of the PSCs. **Figure 24**a shows the effect of large forward bias preconditioning before making the $J-V$ measurement. Large forward preconditioning bias improves the V_{oc} and the FF.[5, 15, 123, 131] The 'bump' in the photocurrent as shown in **Figure 21**b is also observed during FR scans with forward bias preconditioning.

Figure 24b shows the effect of reverse bias preconditioning. In this case, the FR scan generally shows higher J_{sc} and FF compared to the RF scan. For large reverse biases, this loss in J_{sc} and FF for the RF scan is pronounced, similar to **Figure 21**d.[123, 124] In some cases, the V_{oc} is severely deteriorated depending on the value of the preconditioning bias.[5] In

addition, extra effects such as inverted hysteresis can be obtained when prior bias is applied, as subsequently discussed in Section 6.5.

The effect of illumination time and intensity on the performance of perovskite solar cells is shown in **Figure 24**c and **Figure 24**d respectively. Prolonged light soaking gradually improves the device performance metrics of efficiency, FF and V_{oc}.[15, 132, 133] The short-circuit current has not been seen to vary significantly. The effect of changing light intensity does not affect the shape of the hysteresis. Note that the 'bump' scales with the light intensity as shown in the normalized curves of **Figure 24**d.[5]

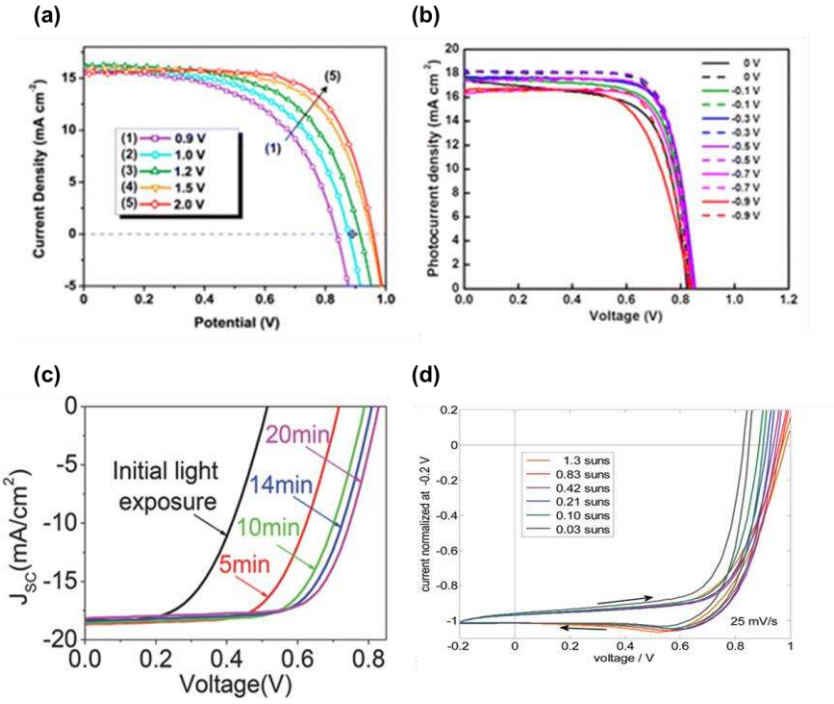

Figure 24. (a) FR scan of planar configuration $MAPbI_3$ cells under different pre-bias forward voltages as shown in legend. The black diamond represents stabilized V_{oc} when holding the device under 1 sun illumination for 60 seconds. Adapted with permission.[123] Copyright 2015, American Chemical Society. (b) FR (dashed lines) and RF (solid lines) curves for $MAPbI_3$ cells with mesoporous TiO_2 scaffold preset at various reverse biases in the dark for 5 minutes (Forward to reverse (FR) and reverse to forward (RF) bias). Adapted with permission.[124] Copyright 2014, American Chemical Society. (c) Effect of light soaking at 1

sun illumination on inverted ITO/PEDOT/$MAPbI_3$/PCBM/Au samples. Adapted with permission.[132] Copyright 2015, John Wiley & Sons. (d) Effect of light intensity on hysteretic behavior of $MAPbI_3$ cells with mesoporous TiO_2 scaffold. Adapted with permission.[5] Copyright 2015, Royal Society of Chemistry.

In addition to hysteresis in $J-V$ curves, the effects of light soaking manifest themselves in several other experiments as well and provide strong insights into the operation of the perovskite solar cell. Hu et al.[92] observed that the magnitude of the V_{oc} for a given light intensity was reduced for a light-soaked $MAPbI_{3-X}Cl_X$ solar cell compared to when it was in dark storage. This reduction was minimized for cells with an Al_2O_3 scaffold. Zhang et al.[134] identified that the evolution towards a steady state V_{oc} was much faster in the case of light soaked cells compared to cells that were not kept in dark storage. These light soaking effects have been found to be reversible, with the cells regaining their original pre-soaking behavior upon extended dark storage. Similar trends have been observed from EQE measurements,[135] where 30 minutes of light soaking yielded a 50% drop from the EQE of an un-soaked device, followed by a recovery to 90% of the initial value upon extended dark storage. Furthermore, Shao et al.[136] (subsequently by Zhang et al.[134]) identified that replacing PCBM with PTEG-1 as the electron selective contact in inverted $MAPbI_{3-X}Cl_X$ cells eliminates the light soaking effect, indicating the importance of the external contacts for this effect. These observations in addition to the remnant V_{oc} observed over long timescales (see **Figure 13**) and light intensity-dependent large low frequency capacitance (see **Figure 19**) have been interpreted as the accumulation of electronic carriers at the perovskite/ESL contact, where surface recombination could explain the observed trends, as proposed by Bisquert and co-workers. This model is further discussed in Section 6.4.

Hysteresis in *J-V* curves is also strongly dependent on temperature. For instance, it has been observed to increase for temperatures below room temperature,[14, 120, 137] as shown in **Figure 25**. Bryant et al.[138] also observed a similar trend for fullerene top cathode $MAPbI_3$ cells

which are virtually hysteresis-free at room temperature. They observed an increase in the timescale of the slow relaxation process as the temperature decreased, with hysteresis disappearing at 77 K. From chronoamperometry measurements, they calculated an Arrhenius behavior for the photocurrent decay half-times, yielding an activation energy of 0.12 eV for this process. Both Bryant et al. and Zou et al.[139] identified that the performance of the cell was maximized under pre-biasing at a large forward bias at low temperatures, where the low temperature 'freezes' the favorable condition of the pre-biasing. In general, the hysteresis is maximized when the timescale of the slow relaxation process is similar to the timescale of the $J-V$ measurement. By correlating the slow, temperature-activated process to the low frequency time constant observed in impedance spectroscopy measurements at different temperatures, Contreras et al.[14] were also able to estimate activation energies of the slow process based on an Arrhenius-type equation, which they attributed to the ionic diffusion process.

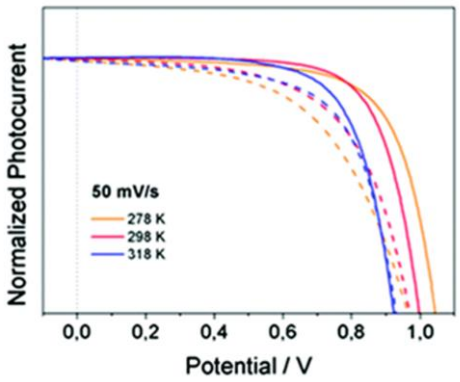

Figure 25. $J-V$ curves of $CH_3NH_3PbI_3$ solar cells with mesoporous TiO_2 scaffold at different temperatures under 10 $mW \cdot cm^{-2}$ illumination using a green LED. Solid lines and dashed lines represent FR and RF scans respectively. Adapted with permission.[14] Copyright 2016, Royal Society of Chemistry.

Another unique and extreme case of the hysteretic phenomena described in the previous section is that of the switchable photovoltaic effect. This effect was observed by Xiao[16] and

coworkers for inverted configuration perovskite samples consisting of ITO/PEDOT:PSS/$MAPbI_3$/Au. They observed that depending on the poling bias, the sign of the photovoltage and photocurrent could be switched to either positive or negative, allowing photovoltaic operation in either bias direction, which is an extreme case of the pattern of **Figure 21**d.

6.4. Hysteresis interpretation: two main models

Due to the complex nature and range of dynamic hysteresis trends and their sensitivity to materials and methods, a general all-encompassing model that accounts for these trends has been very difficult to achieve. Several general mechanisms have been proposed to explain the dynamic hysteresis in perovskite solar cells, such as ionic motion, ferroelectric effects,[17, 124, 130] displacement currents due to depolarization of ionic accumulation[126] and unbalanced electron and hole fluxes[140] due to inefficient charge extraction and subsequent transport in the TiO_2 layer.[141-144]

We can summarize two models in the current literature that systematically capture several dynamic hysteresis trends based on the specific experimental routines. These models are shown in **Figure 2**e and **Figure 26** and described in the subsequent paragraphs.

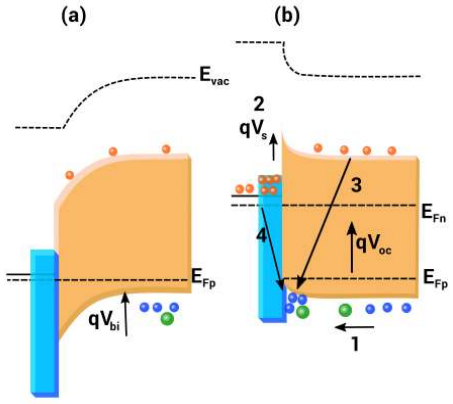

Figure 26. (a) Schematic diagram of the compact TiO_2 (blue layer)/perovskite (orange film) interface indicating the processes governing the V_{oc}. We consider a p-type perovskite at SC condition with a built-in potential at the perovskite/c-TiO_2 interface (electrons represented

in red, holes and cations in blue and green respectively). (b) The PSC at large forward bias. Process (1) indicates the kinetics of drift of cations and holes towards the interface. The accumulation of cations and holes at the interface creates an upward band bending which can be described by a surface voltage V_s represented in (2). These accumulated charges can act as a preferential zone for both recombination with electrons in the bulk (3) and in the c-TiO_2/FTO region. Recombination of electrons at the contact (4) is a crucial mechanism controlling recombination rates of surface accumulated charges and the output V_{oc} in a transient scan.

The first model,[5, 9] as has also been described in Section 3, is based on variations in the charge collection efficiency of the perovskite solar cell throughout a *J-V* scan. This model considers the device as a p-i-n solar cell with a built-in electrical field through the device that is the difference in the work functions between the two contacts. This electrical field controls the transport of the photogenerated carriers to the respective selective contacts and their recombination, depending upon the applied voltage, which modifies the electrical field. The mobile cations and anions in the perovskite cell drift along the built-in potential, forming space charge layers at the contacts that effectively shield or screen the net electric field, creating a bulk field-free region with sharp potential drops at the contacts in the dark at equilibrium, as shown in **Figure 2**e. From this situation, depending on the scanning direction, charge collection is either favored (FR) or deterred (RF). Under applied forward bias, the bands tilt , creating an electrical field that is unfavorable for extracting photogenerated electrons and holes at ESL and HSL respectively, causing recombination of electron-hole pairs. Upon moving from equilibrium, the amount of screening or compensation of the bulk electrical field under applied bias is modulated by the slow drift of the ions towards the respective contacts due to the applied voltage.

Simulations based on this model capture the capacitive behavior with respect to scan rate as

shown in **Figure 21**a, with the bulk electrical field compensated through the scan at very low scan rates, leading to low hysteresis, intermediate scan rates showing large hysteresis and high scan rates not giving enough time for redistribution of the ions and hence low hysteresis.[19] This model also obtains the 'bump' in the photocurrent of **Figure 21**b and the strong decay of photocurrent (**Figure 21**d) and V_{oc} in the RF direction.

Further support for the charge collection effect in the measurements of dynamic hysteresis can be introduced by combining step voltage measurements with transient photocurrent decay measurements. This was carried out by Calado et al.[47] and Belisle et al.[9] in the form of step-dwell-probe (SDP) and step-dwell-step-probe (SDSP) measurements. The SDP measurement (**Figure 27**a) involves a voltage step (V_d) from equilibrium, followed by a waiting period (dwell time), upon which a square wave pulse is applied and the photocurrent decay is measured. The SDSP measurement (**Figure 27**b) involves another voltage step termed the probe voltage (V_p). The authors observed currents opposite to extracted photocurrent for forward voltages (0.3 V) much smaller than the built-in potential of the perovskite, see **Figure 27**c, indicating the compensation of the bulk field. The role of the slow migration of ions in the shielding is reinforced by the shift in the onset of the extracted photocurrent density for larger dwell times in an SDSP experiment, **Figure 27**d.

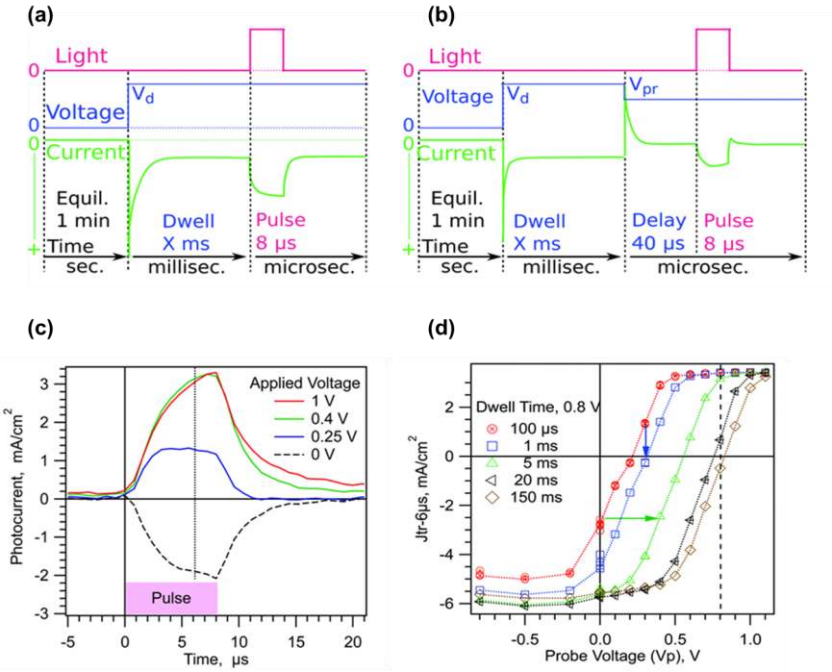

Figure 27. Schematic of (a) step-dwell-probe (SDP) method and (b) step-dwell-step-probe (SDSP) method with corresponding timescales shown. (c) shows the current transients for different step voltages V_d in a SDP experiment on planar $MAPbI_3$ samples. (d) shows the corresponding SDSP measurement for the same sample for different dwell times as shown in the legend. Adapted with permission.[9] Copyright 2017, Royal Society of Chemistry.

The second model, which is in our opinion a more relevant model that captures the hysteretic trends of the perovskite solar cell, is based on interfacial polarization and recombination, starting from a surface polarization model.[2] The central support for this approach comes from the well-known fact that the dynamic hysteresis is closely related to the nature of the contacts used.[145, 146] This information was apparent from the fact that inverted perovskite structures showed much lower hysteresis compared to regular planar or mesoporous scaffold configurations. In addition, depending on the nature of the contact, the hysteresis trends and their characteristic times are also observed to be altered,[15] indicating a strong dependence of hysteresis on the interfacial properties of the device. A deeper study into the contact properties of the perovskite solar cell from IS measurements revealed a strong

connection between the large low frequency capacitance under illumination and the degree of hysteresis observed, where the low frequency capacitance in the dark and under illumination was reduced substantially upon replacing c-TiO_2 with a [6,6]-phenyl C_{61} butyric acid methyl ester (PCBM) layer.[56] The capacitive nature of the TiO_2/perovskite interface has been attributed to the reversible accumulation of I^- ions at this interface due to weak Ti-I-Pb bonds, where measurements on symmetric TiO_2/$MAPbI_3$/TiO_2 and Spiro-OMeTAD/ $MAPbI_3$/Spiro-OMeTAD samples clearly showed reversible capacitive currents only for the symmetric TiO_2/$MAPbI_3$/TiO_2 device.[43] Therefore, the chemical and capacitive properties of the interfaces in a perovskite solar cell, specifically the TiO_2/perovskite interface, has been deemed critical for the hysteresis in the device.

The surface polarization model considers a p-type perovskite with respective selective contacts as shown in **Figure 26**. Note that the transport of carriers in the perovskite is predominantly diffusive and is considered to be excellent and hence, the Fermi levels are flat throughout the perovskite.

Under applied forward bias, an accumulation layer of cations and holes is created at the TiO_2/perovskite interface, creating an upward band bending with an excess surface potential. Upon voltage cycling, this surface potential relaxes, causing a capacitive discharge of the accumulated holes in the form of an extracted photocurrent. However, this capacitive discharge is delayed by the slow transport of the accumulated ions away from the interface. This model reproduces several of the observed features of dynamic hysteresis in the FR direction such as the 'bump' of **Figure 21**b, the photocurrent trends of **Figure 21**c and the apparent shunt resistance effect observed in some cases. The validity of the formation of an accumulation layer at the TiO_2/perovskite interface is based on detailed drift-diffusion simulations[8] and strong experimental evidence, including a large low frequency capacitance of the order of mF that scales with light intensity as detailed earlier, and an unbalanced distribution of charge in the perovskite with an excess density of positive charge at the TiO_2/perovskite interface under illumination, from KPFM.[147] The slow discharge of the

accumulated holes is also consistent with the observation of a remnant V_{oc} over large timescales as commented earlier. This model successfully reproduces several of the anomalous spectra observed from IS, including the observation of a negative capacitance (**Figure 20**) at intermediate to low frequencies.[117]

The origin of the collection model is related to the initial stages of development of the perovskite solar cell, where the hysteretic trends were dominated by variations in the photocurrent density, as seen in **Figure 21**. This allowed simply modeling the perovskite solar cell with transport limitations similar to an organic solar cell, with an electric field through the bulk. However, state-of-the-art perovskite solar cells with high efficiencies show excellent charge transport features, as will be detailed in Section 6.6. Therefore, the influence of an electrical field that facilitates transport should be minor, unless working in large reverse bias conditions. The strong correlation between the contact capacitance and the hysteretic trends indicates that variations in V_{oc} governed by specific recombination mechanisms will be the distinguishing factor for hysteresis in high quality, state-of-the-art perovskite solar cells.

Furthermore, the charge collection model does not account for some global observations of the properties of the perovskite solar cell.

The first is the strong dependence on contacts mentioned before; the effect of the contacts in this model actuates only through the work function and built-in voltage, and a correlation between these and hysteresis is not demonstrated. The dynamic hysteresis correlates with the surface capacitance rather than the energetic properties of the contact. Secondly, the approximation of sheets of ionic charge at the contacts[3, 9, 66] in narrow Debye layers close to the interfaces that compensate the electrical field is erroneous as this distribution does not produce a flat electrochemical potential of the ions. Allowing for this consideration leads to a partially compensated electrical field, rather than a complete compensation,[61] as seen from **Figure 5** and discussed extensively in Section 3. Moreover, the distinct recombination features observed from open-circuit voltage decays, where a remnant V_{oc} was observed over a

timescale of seconds,[8, 89, 91] in unison with the observation of a large low frequency capacitance from impedance spectroscopy measurements that scales with light intensity[55] (**Figure 19**), much higher than the limit of an ionic Helmholtz double layer capacitance,[7] are unaccounted for in this model.

Therefore, we can conclude that under extreme forcing by external bias, major reorganization of ions can produce a severe electrical field which may cause effects of variation of photocurrent and even inverted hysteresis, as discussed in the next section. This is especially the case for low quality perovskite solar cells, where charge collection properties are poor and can be modified significantly by the ions.

However, under normal operation of high performance perovskite solar cells, the charge collection properties are excellent and hence, the observed dynamic hysteresis is dominated by the effect of the contacts by a combination of two factors: (a) The charge accumulation at contacts, governed by surface capacitance that depends on state of illumination and bias and (b) The slow reorganization response, governed by the interplay of charge accumulation and recombination.

6.5. Inverted hysteresis and non-capacitive currents

So far, as noted earlier, most of the $J-V$ curve hysteretic patterns evidence a clear advantage in reporting the FR scan direction in which, generally, larger J_{sc} and/or FF and hence PCE are attained, in comparison with the RF bias sweep. Without considering further specific features, this has been known as "normal" hysteresis (NHys).

However, just the opposite behavior was reported by Tress et al.[125] from *J-V* curves of mixed perovskite-based cells after 1.2 V forward biasing for 10 s. As illustrated in **Figure 28**, an S-shape significant reduction of the current around the operation voltage region diminishes FF, and hence PCE, during the FR scan with respect to RF. Note that here, HI<0 around the operation voltage (Equation (24)), differently to NHys where 0<HI<1. This behavior was

subsequently termed as "inverted" hysteresis (IHys) and their effects were proved to persist at different scan rates, scan loops, prebiasing and illumination intensities. Regarding these latter experiments, **Figure 28** shows the light independent character of the current kink during a FR sweep, which was interpreted as discarding the relation between inverted hysteresis and charge extraction barriers due to photogenerated charges. In addition, they also found inverted hysteresis in $MAPbI_3$ devices with a mesoporous TiO_2 scaffold covered with a thin insulating Al_2O_3 shell. They attributed this observation to the existence of a barrier for electron extraction at the TiO_2/perovskite interface in their cells, where charge extraction is favoured at 0 V (SC) instead of at large forward bias due to negative accumulated ionic charge at the TiO_2/perovskite interface at short-circuit, which creates a dipole that allows for band alignment.

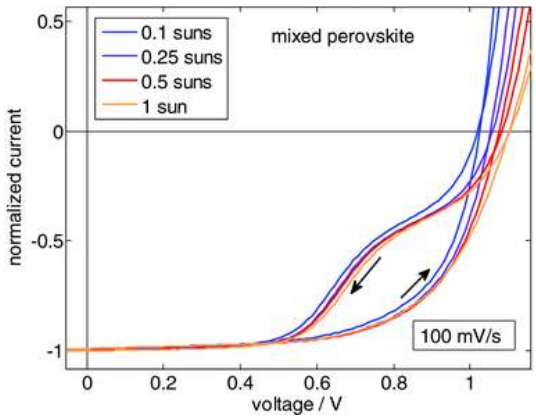

Figure 28. Inverted hysteresis in *J-V* curves of mixed perovskite-based devices at different illumination intensities. Reprinted with permission.[125] Copyright 2016, John Wiley & Sons.

Interestingly, subsequent reports on IHys[107, 126, 148, 149] focused on less exotic perovskites that did not include the S-shape of the measurements by Tress and co-workers. Shen et al.[148] defined inverted hysteresis predominantly in the form of variations in the J_{sc} of their cells upon strong F poling, where the J_{sc} of the FR scan changed from being higher to lower than that of the RF scan when moving from slow to fast scan rates. Moreover, the effect was apparently dependent on the fabrication procedure, which was understood as an effect of

different $MAPbI_3$ electron affinities. In this sense, they suggested that in some devices, ion accumulation occur at large forward biases, producing a temporary and localized increase in recombination at the $MAPbI_3/TiO_2$ interface, leading to inverted hysteresis at fast scan rates. Such a hypothesis was also supported by numerical semiconductor models including ion accumulation where two possible origins for these localized recombination losses were proposed: one based on band bending and the other on an accumulation of ionic charge in the perovskite bulk.

Recently, an analysis of hole-conductor-free printable cells with a triple-layer architecture of TiO_2/ZrO_2/Carbon,[129] has shown new features of the dynamic hysteresis in robust and stable perovskite solar cells, as presented in **Figure 29**. The changes of hysteresis patterns are caused exclusively by a tuning of the TiO_2 compact layer, which speaks of the dominant role of charge accumulation at this interface. Furthermore, the appearance of NHyst, hysteresis free and IHyst, affects only the voltage, as mentioned before in connection with **Figure 25**, while charge collection at short circuit is virtually the same in all cases. These physical features have been explained by an extension of the original surface polarization model[2] that considers in addition the rate of surface recombination that is modified by the quality of the TiO_2 blocking layer.

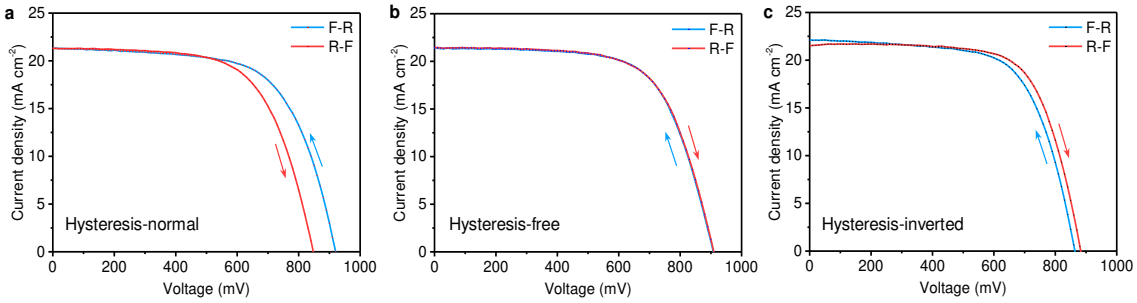

Figure 29. $J-V$ curves of printable mesoscopic PSCs with different hysteresis behaviors. (a) Hysteresis-normal device whose F-R scan shows better performance than R-F scan; (b) Hysteresis-free device whose F-R scan and R-F scan show non-distinctive performance; (c) Hysteresis-inverted device whose F-R scan shows slightly lower performance than R-F scan.

Scan rate 250 mV s^{-1}. Reprinted with permission.[129] Copyright 2017, Royal Society of Chemistry.

An approach more focused on the influence of pre-biasing, also known as pre-poling, was made by Nemnes et al.[126], who measured TiO_2/$MAPbI_{3-x}Cl_x$/spiro-OMeTAD based devices in the continuous sequence FR-RF-FR after bias pretreatment. They verified that NHys typically appears at pre-poling biases larger than V_{oc}, while pronounced IHys occurs for adequate negative bias pre-poling. These observations are in close relation to the J_{sc} response of **Figure 14**. Interestingly, they also showed dark $J-V$ curves with the occurrence of these trends.

Contrastingly, dark IHys as above defined was found by Almora and co-workers[107, 128] at slow scan rates without pre-biasing in several device configurations (see **Figure 22**a). The appearance of this feature when approximating quasi-steady state measurements suggested additional non-capacitive charge extraction mechanisms, possibly due to reversible reactivity. As shown in **Figure 1**f, the drift of ions due to polarization catalyzes reactivity processes, which act similarly to pre-biasing during slow voltage sweeps. Importantly, it was remarkably noticeable in devices with organic selective contacts. The latter was also supported by Erdenebileg et al.,[149] who found very small IHys under illumination at slow scan rates in others cells with organic materials comprising the perovskite. They however attributed this feature to a build-up of a space-charge region at the ESL–perovskite interface.

6.6. Other factors affecting hysteresis and its suppression

Another prominent interpretation of the dynamic hysteresis involves trapping and detrapping effects. As in other solar cells, the presence of traps can affect the PSC performance, modifying the magnitude of the current density and the shape of $J-V$ curves.[150-152] Minemoto & Murata[153] identified the contribution of the defect density at the

front interface to the hysteresis as much stronger than that at the back interface for large absorption coefficient materials (such as PSCs) without considering ion migration, though they did not implement dynamic scans. Other authors include both charge trapping and ion migration in numerical modeling,[4, 62, 63] where the distribution of ions can significantly alter the collection properties of the device. In fact, Van Reenen et al.[62] suggested that the relatively high rate of recombination at the interface is sustained by large electron and hole densities due to (i) electronic compensation of ionic space charge and (ii) electronic traps. Neukom et al.[63] reproduced NHhys trends by considering variations in surface recombination and diffusion lengths of the carriers in addition to ionic migration. Similar conclusions have been reported by Sherkar et al.[154, 155] in their study of recombination employing drift-diffusion simulations, who suggested that there is a direct correlation between the density of trap states, the density of mobile ions, and the degree of hysteresis observed in the current-voltage curves.

While the effects of trapping-detrapping cannot be ruled out, the magnitude of the low frequency capacitance observed from IS measurements, where the response from traps is generally observed, is extremely large and is known to scale exponentially with light intensity and large forward bias, as seen from **Figure 19** and **Figure 15** respectively, and therefore cannot be ascribed to a density of traps. Furthermore, the slow transients in the timescale of seconds indicates detrapping rates at the same timescale, which is unrealistic, casting further doubt on the validity of trapping-detrapping effects having a significant impact on the dynamic hysteresis trends.

Another important aspect contributing to the dynamic hysteresis is the modification of injection/extraction barriers at the perovskite interface due to reorganization of mobile ions, as described earlier. These modifications can cause large changes in the extraction capability of the cell (see **Figure 14**), which can lead to dynamic hysteresis. It is well known that the use of organic contacts such as PCBM suppresses the dynamic hysteresis. Several authors also correlate the reduced hysteresis with the improved charge transport and extraction properties

of fullerene-incorporated perovskite devices[58, 59] as compared to TiO_2-based perovskite devices. As will be seen subsequently, these injection/extraction barriers are highly dependent on the nature of the contacts used and strongly affect the hysteretic trends.

Figure 30a and **Figure 30**b show $J-V$ curves of a high efficiency, bulk heterojunction perovskite-PCBM device, which is hysteresis-free under different scan speeds and direction. The fullerene is incorporated either as a planar layer or is mixed into the perovskite layer in a bulk heterojunction form.[156, 157] Xu et al.[157] tested several ratios of perovskite:PCBM hybrid devices and observed a monotonic increase in the transient PL quenching efficiency with increasing perovskite:PCBM ratio, as shown in **Figure 30**c, which was attributed to the increased carrier extraction efficiency for the hybrid devices. However, for extremely high concentrations of PCBM, the quenching reduced greatly (**Figure 30**c, black line). In addition, thermal admittance spectroscopy measurements on perovskite and perovskite:PCBM samples showed a large reduction in the shallow trap density for perovskite:PCBM samples as shown in **Figure 30**d, which was further corroborated by a blue shift in PL emission for perovskite:PCBM samples.[10]

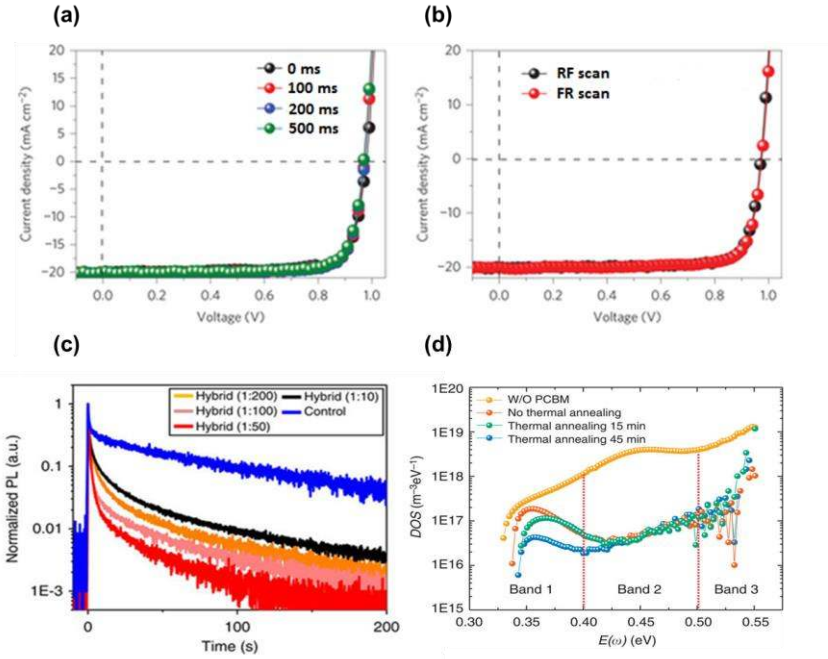

Figure 30. $J-V$ curves of bulk heterojunction $MAPbI_3$-PCBM cells indicating (a) the effect of different scan speeds with delay times given in inset and (b) scanning direction (Forward to reverse (FR) and reverse to forward (RF) bias). (a) and (c) reprinted with permission.[156] Copyright 2016, Macmillan Publishers Ltd on behalf of Cancer Research UK: Nature Photonics. (c) Transient PL of $MAPbI_3$-PCBM hybrid cells for increasing PCBM ratio progressively (orange, pink, red and black) compared to a control film (no PCBM, blue). Reprinted with permission.[157] Copyright 2015, Macmillan Publishers Ltd under CC BY 4.0 license. (d) trap density of states (t-DOS) obtained from thermal admittance spectroscopy measurements for samples without PCBM and with PCBM for different annealing times as indicated in the inset. The bands indicate the different regions (deep traps and shallow traps) influenced by the thermal annealing and PCBM. Reprinted with permission from Macmillan Publishers Ltd: Nature Communications [10], copyright 2014.

Several other studies have also shown the improved carrier transport and extraction properties for perovskite cells with PCBM layers as ESL and perovskite:PCBM hybrid devices from intensity modulated photovoltage spectroscopy (IMPS) measurements,[144] transient photocurrent measurements[10, 156] and PL decay measurements.[59, 144, 158] The faster decays of photocurrent and quenching of PL in fullerene-incorporated devices in these cases have clearly shown that charge transfer/extraction at the PCBM/perovskite interface is significantly faster than that of the TiO_2/perovskite interface. The use of C_{60}-PCBM as the ESL in planar cells has also been observed to increase the efficiency of charge extraction from transient absorption measurements.[159] These results indicate that charge extraction at interfaces can be a significant factor in the hysteretic properties of a perovskite solar cell and subsequent models must take this into account to develop a holistic model.

While the mechanisms of dynamic hysteresis are being strongly debated, it is well known that the origin of the hysteresis is strongly linked to the migration of ions through the perovskite lattice. Therefore, strategies to suppress hysteresis have been mainly focused on

blocking ion migration channels, namely bulk point defects and grain boundaries,[160] in addition to trap passivation. The most successful and prominent ones are the incorporation of fullerene in contacts/blend form, and improvement of crystalline quality of the perovskite absorber. We discuss these two strategies in detail in the subsequent paragraphs, while touching on several related hysteresis suppression techniques.

The beneficial effect with respect to minimizing hysteresis by the incorporation of fullerenes such as PCBM in the perovskite solar cell has generally been attributed to passivation of traps in the bulk or at the surfaces.[10, 156, 157] Furthermore, it has been proposed that PCBM can tie up iodide-rich surface sites or simply iodide anions, preventing the migration of anions through the perovskite,[157] or more generally, filling defects at grain boundaries that allow the migration of ions through the device.[161]

The role of grain boundaries in facilitating the migration of ionic species within the perovskite has in fact been confirmed from sophisticated conductive-atomic force microscopy (c-AFM) measurements that allow measurement of hysteretic currents at regions close to and far from grain boundaries.[161] In order to reduce the bulk defect density and to minimize the effect of grain boundaries on the hysteretic properties of the device, several attempts have also been made to improve the quality of the perovskite absorber by increasing the grain size of the crystals. To this end, high performance cells with micrometer-sized grains have been reported.[162-164] Xiao et al.[165] observed that inverted $MAPbI_3$ cells obtained from a solvent-annealing (SA) procedure yielded large grain sizes of the order of micrometers. These cells showed higher performance and negligible hysteresis at room temperature compared to samples obtained from thermal annealing (TA), with average grain sizes of a few hundred nanometers. The authors also carried out thermal admittance spectroscopy measurements which showed a much lowered defect density for SA samples compared to TA samples, resulting in rapid charge extraction and larger lifetimes observed from photocurrent and photovoltage decay measurements respectively.

The effect of annealing also appears to lower the density of deep trap states as shown in

Figure 30d. Shao et al.[161] also observed similar results, with SA samples showing reduced dark hysteresis properties. A systematic study by Park et al.[113] with different crystal grain sizes for planar $MAPbI_3$ cells also identified that the hysteresis reduced strongly with increasing grain size of the absorber.

In an extreme scenario, Nie et al.[166] showed the absence of hysteresis (**Figure 31**a, **Figure 31**b) in high efficiency inverted PSCs with the grain size of the absorber in the range of millimeters. From Hall measurements, they observed that the mobility showed a four-fold improvement when the grain size was increased from 100 to 170 micrometers, see **Figure 31**c. They also identified that the dominant recombination pathway was band-to-band bimolecular recombination, as can be seen from the slope of the evolution of V_{oc} vs. light intensity in **Figure 31**d and also from time-resolved PL measurements on small and large grains, typical of high quality devices. Therefore, the reduced hysteresis has been generally linked with the improved carrier transport properties for high crystallinity devices.

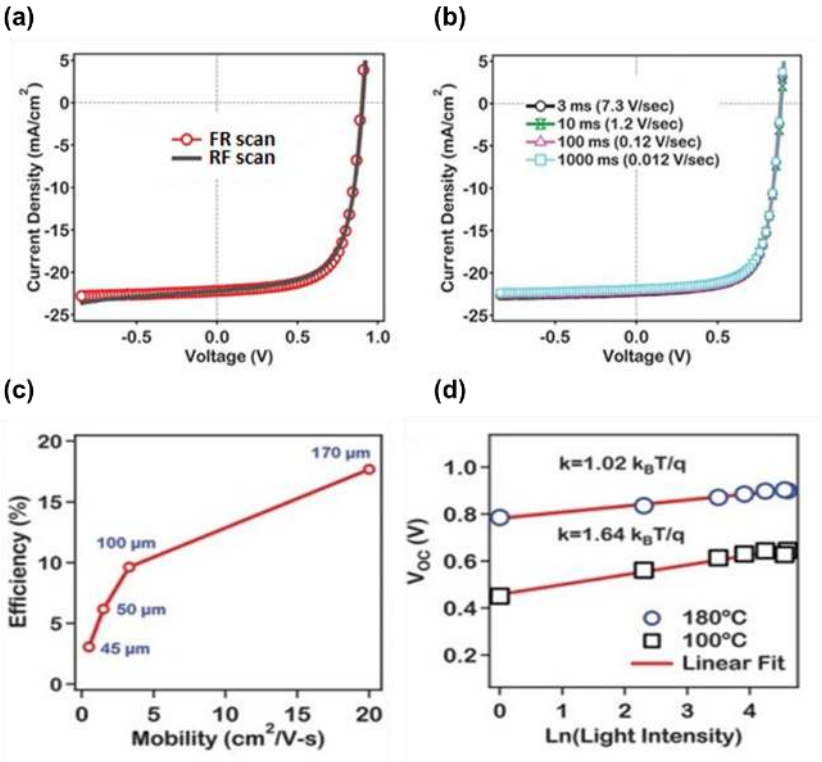

Figure 31. $J-V$ curves for different (a) scan direction (Forward to reverse (FR) and reverse to forward (RF) bias) and (b) scan rate for inverted PSCs with millimeter-sized grain size for the absorber. (c) shows the calculated mobility from Hall measurements and (d) shows the trend of V_{oc} versus light intensity for two grain sizes in terms of their annealing temperature (larger temperature has the larger grain size), with corresponding linear fits and their respective slope k. Adapted with permission.[166] Copyright 2015, AAAS.

However, a recent study by Peng et al.[167] has strongly questioned the influence of grain boundaries in the observed hysteresis. The authors prepared high efficiency, monocrystalline $MAPbBr_3$ devices with and without ESL and HSL. They observed strong hysteresis in cells without an ESL and HSL, which was significantly reduced upon addition of TiO_2 as the ESL. Since the monocrystalline absorber has an ultra-low bulk trap density and is devoid of grain boundaries by definition, it is apparent that there exist further factors that contribute to the hysteretic behavior such as bulk ion migration, which could consequently create a need to alter the chemical structure of the perovskite itself. Increasing valence charges of the ions and co-doping cations with higher and lower valence ions have been proposed in this regard.[168]

Recent strategies to minimize dynamic hysteresis involve the modification or treatment of the TiO_2 layer, which has been deemed critical for the operation of the perovskite solar cell. A novel strategy to eliminate dynamic hysteresis involves the use of Cl-capped TiO_2 nanoparticles at the ESL. These cells showed extremely high performance and stability, coupled with the absence of dynamic hysteresis trends. The Cl-capped TiO_2 nanoparticles were shown to double the charge carrier recombination lifetime of ordinary TiO_2 based cells, thereby connecting the reduction in dynamic hysteresis to the passivation of surface traps at the TiO_2/perovskite contact.[169] Based on similar reasoning, perovskite solar cells based on Li-treated mesoscopic TiO_2 have been shown to be hysteresis-free, attributed to the improved charge extraction properties observed from photoluminescence decays upon Li treatment

compared to untreated TiO_2.[170]

7. Conclusions

The emergence and consolidation of perovskite solar cells has opened a wide new field of study in photovoltaics. Perovskites solar cells are distinguished by a very broad set of peculiar physical properties with respect to former kinds of solar cells. In this review, we have addressed the connection between fundamental properties and device models that allow us for the interpretation of macroscopic measurements in the time and frequency domain. It is widely recognized that the perovskite cells display a rich and very complex phenomenology. Two major factors have contributed to the improved understanding, one is the enhancement of quality of materials and devices, that now allows focusing on the characterization of specific phenomena, and the second is the already very big size of a cooperative community, that has given rise to emerging regularities. However, the presence of many morphologies, mixed ionic-electronic conduction, and organic components of the device, makes the problems yet very open. Despite the great deal of advances in characterization methods and understanding of basic properties, there is a long way to go yet.

Supporting Information

Supporting Information is available from the Wiley Online Library or from the author.

Acknowledgments

We acknowledge funding from MINECO of Spain under Projects MAT2016-76892-C3-1-R and MAT2016-76892-C3-3-R, and Generalitat Valenciana Project PROMETEOII/2014/020. We also acknowledge J. Beloqui and Emilio Palomares for their valuable comments. S.R. and O.A. acknowledge Generalitat Valenciana for Grants GRISOLIA/2014/034 and GRISOLIA/2014/035, respectively.

Received: ((will be filled in by the editorial staff))
Revised: ((will be filled in by the editorial staff))
Published online: ((will be filled in by the editorial staff))

References

[1] H. J. Snaith, A. Abate, J. M. Ball, G. E. Eperon, T. Leijtens, N. K. Noel, S. D. Stranks, J. T.-W. Wang, K. Wojciechowski, W. Zhang, *J. Phys. Chem. Lett.* **2014**, *5*, 1511.

[2] S. Ravishankar, O. Almora, C. Echeverría-Arrondo, E. Ghahremanirad, C. Aranda, A. Guerrero, F. Fabregat-Santiago, A. Zaban, G. Garcia-Belmonte, J. Bisquert, *J. Phys. Chem. Lett.* **2017**, *8*, 915.

[3] D. A. Jacobs, Y. Wu, H. Shen, C. Barugkin, F. J. Beck, T. P. White, K. Weber, K. R. Catchpole, *Phys. Chem. Chem. Phys.* **2017**, *19*, 3094.

[4] S. E. J. O'Kane, G. Richardson, A. Pockett, R. G. Niemann, J. M. Cave, N. Sakai, G. E. Eperon, H. J. Snaith, J. M. Foster, P. J. Cameron, A. B. Walker, *J. Mater. Chem. C* **2017**, *5*, 452.

[5] W. Tress, N. Marinova, T. Moehl, S. M. Zakeeruddin, M. K. Nazeeruddin, M. Gratzel, *Energy Environ. Sci.* **2015**, *8*, 995.

[6] C. Eames, J. M. Frost, P. R. F. Barnes, B. C. O'Regan, A. Walsh, M. S. Islam, *Nat. Commun.* **2015**, *6*, 7497.

[7] E. J. Juarez-Perez, R. S. Sanchez, L. Badia, G. Garcia-Belmonte, Y. S. Kang, I. Mora-Sero, J. Bisquert, *J. Phys. Chem. Lett.* **2014**, *5*, 2390.

[8] R. Gottesman, P. Lopez-Varo, L. Gouda, Juan A. Jimenez-Tejada, J. Hu, S. Tirosh, A. Zaban, J. Bisquert, *Chem* **2016**, *1*, 776.

[9] R. A. Belisle, W. H. Nguyen, A. R. Bowring, P. Calado, X. Li, S. J. C. Irvine, M. D. McGehee, P. R. F. Barnes, B. C. O'Regan, *Energy Environ. Sci.* **2017**, *10*, 192.

[10] Y. Shao, Z. Xiao, C. Bi, Y. Yuan, J. Huang, *Nat. Commun.* **2014**, *5*, 5784.

[11] H.-S. Duan, H. Zhou, Q. Chen, P. Sun, S. Luo, T.-B. Song, B. Bob, Y. Yang, *Phys. Chem. Chem. Phys.* **2015**, *17*, 112.

[12] J. Beilsten-Edmands, G. E. Eperon, R. D. Johnson, H. J. Snaith, P. G. Radaelli, *Appl. Phys. Lett.* **2015**, *106*, 173502.

[13] O. Almora, I. Zarazua, E. Mas-Marza, I. Mora-Sero, J. Bisquert, G. Garcia-Belmonte, *J. Phys. Chem. Lett.* **2015**, *6*, 1645.

[14] L. Contreras, J. Idigoras, A. Todinova, M. Salado, S. Kazim, S. Ahmad, J. A. Anta, *Phys. Chem. Chem. Phys.* **2016**, *18*, 31033.

[15] E. L. Unger, E. T. Hoke, C. D. Bailie, W. H. Nguyen, A. R. Bowring, T. Heumuller, M. G. Christoforo, M. D. McGehee, *Energy Environ. Sci.* **2014**, *7*, 3690.

[16] Z. Xiao, Y. Yuan, Y. Shao, Q. Wang, Q. Dong, C. Bi, P. Sharma, A. Gruverman, J. Huang, *Nat. Mater.* **2015**, *14*, 193.

[17] R. S. Sanchez, V. Gonzalez-Pedro, J.-W. Lee, N.-G. Park, Y. S. Kang, I. Mora-Sero, J. Bisquert, *J. Phys. Chem. Lett.* **2014**, *5*, 2357.

[18] J. M. Frost, A. Walsh, *Acc. Chem. Res.* **2016**, *49*, 528.

[19] G. Richardson, S. E. J. O'Kane, R. G. Niemann, T. A. Peltola, J. M. Foster, P. J. Cameron, A. B. Walker, *Energy Environ. Sci.* **2016**, *9*, 1476.

[20] A. Walsh, *J. Phys. Chem. C* **2015**, *119*, 5755.

[21] J. M. Azpiroz, E. Mosconi, J. Bisquert, F. De Angelis, *Energy Environ. Sci.* **2015**, *8*, 2118.

[22] N. Vicente, G. Garcia-Belmonte, *Adv. Energy Mater.* **2017**, 1700710.

[23] P. Wang, Y. Guo, S. Yuan, C. Yan, J. Lin, Z. Liu, Y. Lu, C. Bai, Q. Lu, S. Dai, C. Cai, *Res. Chem. Intermed.* **2016**, *42*, 625.

[24] L. Wang, G.-R. Li, Q. Zhao, X.-P. Gao, *Energy Storage Materials* **2017**, *7*, 40.

[25] O. Almora, L. Vaillant-Roca, G. Garcia-Belmonte, *Rev. Cub. Fis.* **2017**, *34*, 58.

[26] N.-G. Park, M. Grätzel, T. Miyasaka, Eds., *Organic-Inorganic Halide Perovskite Photovoltaics: From Fundamentals to Device Architectures*, Springer, Switzerland **2016**.

[27] C. C. Stoumpos, C. D. Malliakas, M. G. Kanatzidis, *Inorg. Chem.* **2013**, *52*, 9019.

[28] T. Baikie, Y. Fang, J. M. Kadro, M. Schreyer, F. Wei, S. G. Mhaisalkar, M. Graetzel, T. J. White, *J. Mater. Chem. A* **2013**, *1*, 5628.

[29] Y. Yasuhiro, N. Toru, E. Masaru, W. Atsushi, K. Yoshihiko, *Appl. Phys. Express* **2014**, *7*, 032302.

[30] Y. Kanemitsu, *J. Mater. Chem. C* **2017**, *5*, 3427.

[31] S. Luo, W. A. Daoud, *J. Mater. Chem. A* **2015**, *3*, 8992.

[32] T.-B. Song, Q. Chen, H. Zhou, C. Jiang, H.-H. Wang, Y. Yang, Y. Liu, J. You, *J. Mater. Chem. A* **2015**, *3*, 9032.

[33] W. E. I. Sha, X. Ren, L. Chen, W. C. H. Choy, *Appl. Phys. Lett.* **2015**, *106*, 221104.

[34] D. Song, P. Cui, T. Wang, D. Wei, M. Li, F. Cao, X. Yue, P. Fu, Y. Li, Y. He, B. Jiang, M. Trevor, *J. Phys. Chem. C* **2015**, *119*, 22812.

[35] A. Senocrate, I. Moudrakovski, G. Y. Kim, T.-Y. Yang, G. Gregori, M. Grätzel, J. Maier, *Angew. Chem., Int. Ed.* **2017**, *56*, 7755.

[36] A. Zohar, I. Levine, S. Gupta, O. Davidson, D. Azulay, O. Millo, I. Balberg, G. Hodes, D. Cahen, *ACS Energy Lett.* **2017**, *2*, 2408.

[37] W. S. Yang, J. H. Noh, N. J. Jeon, Y. C. Kim, S. Ryu, J. Seo, S. I. Seok, *Science* **2015**, *348*, 1234.

[38] Q. Chen, H. Zhou, Y. Fang, A. Z. Stieg, T.-B. Song, H.-H. Wang, X. Xu, Y. Liu, S. Lu, J. You, P. Sun, J. McKay, M. S. Goorsky, Y. Yang, *Nat. Commun.* **2015**, *6*.

[39] J.-W. Lee, D.-J. Seol, A.-N. Cho, N.-G. Park, *Adv. Mater.* **2014**, *26*, 4991.

[40] M. Shirayama, M. Kato, T. Miyadera, T. Sugita, T. Fujiseki, S. Hara, H. Kadowaki, D. Murata, M. Chikamatsu, H. Fujiwara, *J. Appl. Phys.* **2016**, *119*, 115501.

[41] W. Huang, J. S. Manser, P. V. Kamat, S. Ptasinska, *Chem. Mater.* **2016**, *28*, 303.

[42] A. Guerrero, J. You, C. Aranda, Y. S. Kang, G. Garcia-Belmonte, H. Zhou, J. Bisquert, Y. Yang, *ACS Nano* **2016**, *10*, 218.

[43] J. Carrillo, A. Guerrero, S. Rahimnejad, O. Almora, I. Zarazua, E. Mas-Marza, J. Bisquert, G. Garcia-Belmonte, *Adv. Energy Mater.* **2016**, *6*.

[44] J. Bisquert, *Nanostructured Energy Devices: Equilibrium Concepts and Kinetics*, CRC Press Taylor & Francis Group, Boca Raton **2014**.

[45] S. Guarnera, A. Abate, W. Zhang, J. M. Foster, G. Richardson, A. Petrozza, H. J. Snaith, *J. Phys. Chem. Lett.* **2015**, *6*, 432.

[46] A. Walsh, D. O. Scanlon, S. Chen, X. G. Gong, S.-H. Wei, *Angew. Chem., Int. Ed. Engl.* **2015**, *54*, 1791.

[47] P. Calado, A. M. Telford, D. Bryant, X. Li, J. Nelson, B. C. O'Regan, P. R. F. Barnes, *Nat. Commun.* **2016**, *7*, 13831.

[48] W.-J. Yin, T. Shi, Y. Yan, *Appl. Phys. Lett.* **2014**, *104*, 063903.

[49] A. Buin, R. Comin, J. Xu, A. H. Ip, E. H. Sargent, *Chem. Mater.* **2015**, *27*, 4405.

[50] Y. Yuan, J. Chae, Y. Shao, Q. Wang, Z. Xiao, A. Centrone, J. Huang, *Adv. Energy Mater.* **2015**, *5*, 1500615.

[51] K. Domanski, B. Roose, T. Matsui, M. Saliba, S.-H. Turren-Cruz, J.-P. Correa-Baena, C. R. Carmona, G. Richardson, J. M. Foster, F. De Angelis, J. M. Ball, A. Petrozza, N. Mine, M. K. Nazeeruddin, W. Tress, M. Gratzel, U. Steiner, A. Hagfeldt, A. Abate, *Energy Environ. Sci.* **2017**, *10*, 604.

[52] K. Domanski, J.-P. Correa-Baena, N. Mine, M. K. Nazeeruddin, A. Abate, M. Saliba, W. Tress, A. Hagfeldt, M. Grätzel, *ACS Nano* **2016**, *10*, 6306.

[53] D. A. Egger, L. Kronik, A. M. Rappe, *Angew. Chem., Int. Ed. Engl.* **2015**, *54*, 12437.

[54] C. Li, A. Guerrero, Y. Zhong, A. Gräser, C. A. M. Luna, J. Köhler, J. Bisquert, R. Hildner, S. Huettner, *Small* **2017**, *13*, 1701711.

[55] I. Zarazua, J. Bisquert, G. Garcia-Belmonte, *J. Phys. Chem. Lett.* **2016**, *7*, 525.

[56] H.-S. Kim, I.-H. Jang, N. Ahn, M. Choi, A. Guerrero, J. Bisquert, N.-G. Park, *J. Phys.*

Chem. Lett. **2015**, *6*, 4633.

[57] G. Garcia-Belmonte, J. Bisquert, *ACS Energy Lett.* **2016**, *1*, 683.

[58] K. Wojciechowski, S. D. Stranks, A. Abate, G. Sadoughi, A. Sadhanala, N. Kopidakis, G. Rumbles, C.-Z. Li, R. H. Friend, A. K. Y. Jen, H. J. Snaith, *ACS Nano* **2014**, *8*, 12701.

[59] M. De Bastiani, G. Dell'Erba, M. Gandini, V. D'Innocenzo, S. Neutzner, A. R. S. Kandada, G. Grancini, M. Binda, M. Prato, J. M. Ball, M. Caironi, A. Petrozza, *Adv. Energy Mater.* **2016**, *6*, 1501453.

[60] J. M. Foster, H. J. Snaith, T. Leijtens, G. Richardson, *SIAM J. Appl. Math.* **2014**, *74*, 1935.

[61] P. Lopez-Varo, J. A. Jiménez-Tejada, M. García-Rosell, J. A. Anta, S. Ravishankar, A. Bou, J. Bisquert, *ACS Energy Lett.* **2017**, *2*, 1450.

[62] S. van Reenen, M. Kemerink, H. J. Snaith, *J. Phys. Chem. Lett.* **2015**, *6*, 3808.

[63] M. T. Neukom, S. Züfle, E. Knapp, M. Makha, R. Hany, B. Ruhstaller, *Sol. Energy Mater. Sol. Cells* **2017**, *169*, 159.

[64] O. Almora, A. Guerrero, G. Garcia-Belmonte, *Appl. Phys. Lett.* **2016**, *108*, 043903.

[65] P. Lopez-Varo, L. Bertoluzzi, J. Bisquert, M. Alexe, M. Coll, J. Huang, J. A. Jimenez-Tejada, T. Kirchartz, R. Nechache, F. Rosei, Y. Yuan, *Physics Reports* **2016**, *653*, 1.

[66] H. Zhang, C. Liang, Y. Zhao, M. Sun, H. Liu, J. Liang, D. Li, F. Zhang, Z. He, *Phys. Chem. Chem. Phys.* **2015**, *17*, 9613.

[67] J.-P. Correa-Baena, S.-H. Turren-Cruz, W. Tress, A. Hagfeldt, C. Aranda, L. Shooshtari, J. Bisquert, A. Guerrero, *ACS Energy Lett.* **2017**, *2*, 681.

[68] S. De Wolf, J. Holovsky, S.-J. Moon, P. Löper, B. Niesen, M. Ledinsky, F.-J. Haug, J.-H. Yum, C. Ballif, *J. Phys. Chem. Lett.* **2014**, *5*, 1035.

[69] A. Sadhanala, F. Deschler, T. H. Thomas, S. E. Dutton, K. C. Goedel, F. C. Hanusch, M. L. Lai, U. Steiner, T. Bein, P. Docampo, D. Cahen, R. H. Friend, *J. Phys. Chem. Lett.* **2014**, *5*, 2501.

[70] K. Tvingstedt, O. Malinkiewicz, A. Baumann, C. Deibel, H. J. Snaith, V. Dyakonov, H. J. Bolink, *Scientific Reports* **2014**, *4*, 6071.

[71] T. Handa, D. M. Tex, A. Shimazaki, A. Wakamiya, Y. Kanemitsu, *J. Phys. Chem. Lett.* **2017**, *8*, 954.

[72] O. A. Jaramillo-Quintero, R. S. Sanchez, M. Rincon, I. Mora-Sero, *J. Phys. Chem. Lett.* **2015**, *6*, 1883.

[73] Y. Yamada, T. Nakamura, M. Endo, A. Wakamiya, Y. Kanemitsu, *J. Am. Chem. Soc.* **2014**, *136*, 11610.

[74] R. L. Milot, G. E. Eperon, H. J. Snaith, M. B. Johnston, L. M. Herz, *Adv. Funct.*

Mater. **2015**, *25*, 6218.

[75] A. D. Wright, R. L. Milot, G. E. Eperon, H. J. Snaith, M. B. Johnston, L. M. Herz, *Adv. Funct. Mater.*, 1700860.

[76] M. C. Brennan, J. Zinna, M. Kuno, *ACS Energy Lett.* **2017**, *2*, 1487.

[77] C. M. Sutter-Fella, Y. Li, M. Amani, J. W. Ager, F. M. Toma, E. Yablonovitch, I. D. Sharp, A. Javey, *Nano Lett.* **2016**, *16*, 800.

[78] K. T. Cho, S. Paek, G. Grancini, C. Roldan-Carmona, P. Gao, Y. Lee, M. K. Nazeeruddin, *Energy Environ. Sci.* **2017**, *10*, 621.

[79] R. Augulis, M. Franckevičius, V. Abramavičius, D. Abramavičius, S. M. Zakeeruddin, M. Grätzel, V. Gulbinas, *Adv. Energy Mater.*, 1700405.

[80] Z. Liu, J. Hu, H. Jiao, L. Li, G. Zheng, Y. Chen, Y. Huang, Q. Zhang, C. Shen, Q. Chen, H. Zhou, *Adv. Mater.* **2017**, 1606774.

[81] Y. Fang, H. Wei, Q. Dong, J. Huang, *Nature Communications* **2017**, *8*, 14417.

[82] W. Tress, N. Marinova, O. Inganäs, M. K. Nazeeruddin, S. M. Zakeeruddin, M. Graetzel, *Adv. Energy Mater.* **2015**, *5*, 1400812.

[83] J. W. Ryan, E. Palomares, *Adv. Energy Mater.* **2017**, *7*, 1601509.

[84] A. Maurano, C. G. Shuttle, R. Hamilton, A. M. Ballantyne, J. Nelson, W. Zhang, M. Heeney, J. R. Durrant, *J. Phys. Chem. C* **2011**, *115*, 5947.

[85] N. W. Duffy, L. M. Peter, R. M. G. Rajapakse, K. G. U. Wijayantha, *Electrochem. Commun.* **2000**, *2*, 658.

[86] B. C. O'Regan, P. R. F. Barnes, X. Li, C. Law, E. Palomares, J. M. Marin-Beloqui, *J. Am. Chem. Soc.* **2015**, *137*, 5087.

[87] J. M. Marin-Beloqui, L. Lanzetta, E. Palomares, *Chem. Mater.* **2016**, *28*, 207.

[88] N. F. Montcada, J. M. Marín-Beloqui, W. Cambarau, J. Jiménez-López, L. Cabau, K. T. Cho, M. K. Nazeeruddin, E. Palomares, *ACS Energy Lett.* **2017**, *2*, 182.

[89] A. Baumann, K. Tvingstedt, M. C. Heiber, S. Väth, C. Momblona, H. J. Bolink, V. Dyakonov, *APL Mater.* **2014**, *2*, 081501.

[90] H. Nagaoka, F. Ma, D. W. deQuilettes, S. M. Vorpahl, M. S. Glaz, A. E. Colbert, M. E. Ziffer, D. S. Ginger, *J. Phys. Chem. Lett.* **2015**, *6*, 669.

[91] L. Bertoluzzi, R. S. Sanchez, L. Liu, J.-W. Lee, E. Mas-Marza, H. Han, N.-G. Park, I. Mora-Sero, J. Bisquert, *Energy Environ. Sci.* **2015**, *8*, 910.

[92] J. Hu, R. Gottesman, L. Gouda, A. Kama, M. Priel, S. Tirosh, J. Bisquert, A. Zaban, *ACS Energy Lett.* **2017**, *2*, 950.

[93] B. Chen, M. Yang, X. Zheng, C. Wu, W. Li, Y. Yan, J. Bisquert, G. Garcia-Belmonte, K. Zhu, S. Priya, *J. Phys. Chem. Lett.* **2015**, *6*, 4693.

[94] J. Bisquert, F. Fabregat-Santiago, in *Dye-sensitized solar cells*, (Ed: K. Kalyanasundaram), CRC Press, Lausanne (Switzerland) **2010**, 457.

[95] F. Fabregat-Santiago, G. Garcia-Belmonte, I. Mora-Sero, J. Bisquert, *Phys. Chem. Chem. Phys.* **2011**, *13*, 9083.

[96] J. Bisquert, L. Bertoluzzi, I. Mora-Sero, G. Garcia-Belmonte, *J. Phys. Chem. C* **2014**, *118*, 18983.

[97] S. M. Sze, K. K. Ng, *Physics of Semiconductor Devices*, John Wiley & Sons, Hoboken, New Jersey, USA **2007**.

[98] J. Bisquert, *Physical Chemistry Chemical Physics* **2003**, *5*, 5360.

[99] A. Guerrero, G. Garcia-Belmonte, I. Mora-Sero, J. Bisquert, Y. S. Kang, T. J. Jacobsson, J.-P. Correa-Baena, A. Hagfeldt, *J. Phys. Chem. C* **2016**, *120*, 8023.

[100] N. Onoda-Yamamuro, T. Matsuo, H. Suga, *J. Phys. Chem. Solids* **1992**, *53*, 935.

[101] F. Brivio, K. T. Butler, A. Walsh, M. van Schilfgaarde, *Phys. Rev. B* **2014**, *89*, 155204.

[102] C. Lermer, S. T. Birkhold, I. L. Moudrakovski, P. Mayer, L. M. Schoop, L. Schmidt-Mende, B. V. Lotsch, *Chem. Mater.* **2016**, *28*, 6560.

[103] A. Poglitsch, D. Weber, *J. Chem. Phys.* **1987**, *87*, 6373.

[104] T.-Y. Yang, G. Gregori, N. Pellet, M. Grätzel, J. Maier, *Angew. Chem. Int. Ed.* **2015**, *54*, 7905.

[105] O. Almora, C. Aranda, E. Mas-Marzá, G. Garcia-Belmonte, *Appl. Phys. Lett.* **2016**, *109*, 173903.

[106] F. Recart, A. Cuevas, *IEEE Trans. Electron Devices* **2006**, *53*, 442.

[107] O. Almora, C. Aranda, I. Zarazua, A. Guerrero, G. Garcia-Belmonte, *ACS Energy Lett.* **2016**, *1*, 209.

[108] J. Bisquert, G. Garcia-Belmonte, I. Mora-Sero, in *Unconventional Thin Film Photovoltaics*, The Royal Society of Chemistry, **2016**, 57.

[109] J. Bisquert, G. Garcia-Belmonte, A. Guerrero, in *Organic-Inorganic Halide Perovskite Photovoltaics: From Fundamentals to Device Architectures*, (Eds: N.-G. Park, M. Grätzel, T. Miyasaka), Springer International Publishing, Cham **2016**, 163.

[110] C. Tao, J. Van Der Velden, L. Cabau, N. F. Montcada, S. Neutzner, A. R. Srimath Kandada, S. Marras, L. Brambilla, M. Tommasini, W. Xu, R. Sorrentino, A. Perinot, M. Caironi, C. Bertarelli, E. Palomares, A. Petrozza, *Adv. Mater.* **2017**, *29*, 1604493.

[111] I. Gelmetti, L. Cabau, N. F. Montcada, E. Palomares, *ACS Appl. Mater. Interfaces* **2017**, *9*, 21599.

[112] L. Li, F. Wang, X. Wu, H. Yu, S. Zhou, N. Zhao, *J. Phys. Chem. C* **2016**, *120*, 2536.

[113] H.-S. Kim, N.-G. Park, *J. Phys. Chem. Lett.* **2014**, *5*, 2927.

[114] I. Zarazua, G. Han, P. P. Boix, S. Mhaisalkar, F. Fabregat-Santiago, I. Mora-Seró, J. Bisquert, G. Garcia-Belmonte, *J. Phys. Chem. Lett.* **2016**, *7*, 5105.

[115] X. Wu, H. Yu, L. Li, F. Wang, H. Xu, N. Zhao, *J. Phys. Chem. C* **2015**, *119*, 1253.

[116] F. Fabregat-Santiago, M. Kulbak, A. Zohar, M. Vallés-Pelarda, G. Hodes, D. Cahen, I. Mora-Seró, *ACS Energy Lett.* **2017**, *2*, 2007.

[117] E. Ghahremanirad, A. Bou, S. Olyaee, J. Bisquert, *J. Phy. Chem. Lett.* **2017**, *8*, 1402.

[118] A. Todinova, L. Contreras-Bernal, M. Salado, S. Ahmad, N. Morillo, J. Idígoras, J. A. Anta, *ChemElectroChem* **2017**, *4*, 1.

[119] B. Chen, M. Yang, S. Priya, K. Zhu, *J. Phys. Chem. Lett.* **2016**, *7*, 905.

[120] L. K. Ono, S. R. Raga, S. Wang, Y. Kato, Y. Qi, *J. Mater. Chem. A* **2015**, *3*, 9074.

[121] G. A. Nemnes, C. Besleaga, A. G. Tomulescu, I. Pintilie, L. Pintilie, K. Torfason, A. Manolescu, *Sol. Energy Mater. Sol. Cells* **2017**, *159*, 197.

[122] J. P. Correa-Baena, L. Steier, W. Tress, M. Saliba, S. Neutzner, T. Matsui, F. Giordano, T. J. Jacobsson, A. R. Srimath Kandada, S. M. Zakeeruddin, A. Petrozza, A. Abate, M. K. Nazeeruddin, M. Gratzel, A. Hagfeldt, *Energy Environ. Sci.* **2015**, *8*, 2928.

[123] J. A. Christians, J. S. Manser, P. V. Kamat, *J. Phys. Chem. Lett.* **2015**, *6*, 852.

[124] K.-C. Wang, P.-S. Shen, M.-H. Li, S. Chen, M.-W. Lin, P. Chen, T.-F. Guo, *ACS Applied Materials & Interfaces* **2014**, *6*, 11851.

[125] W. Tress, J. P. Correa Baena, M. Saliba, A. Abate, M. Graetzel, *Adv. Energy Mater.* **2016**, *6*, 1600396.

[126] G. A. Nemnes, C. Besleaga, V. Stancu, D. E. Dogaru, L. N. Leonat, L. Pintilie, K. Torfason, M. Ilkov, A. Manolescu, I. Pintilie, *J. Phys. Chem. C* **2017**, *121*, 11207.

[127] G. A. Sepalage, S. Meyer, A. Pascoe, A. D. Scully, F. Huang, U. Bach, Y.-B. Cheng, L. Spiccia, *Adv. Funct. Mater.* **2015**, *25*, 5650.

[128] M. Valles-Pelarda, B. C. Hames, I. García-Benito, O. Almora, A. Molina-Ontoria, R. S. Sánchez, G. Garcia-Belmonte, N. Martín, I. Mora-Sero, *J. Phys. Chem. Lett.* **2016**, *7*, 4622.

[129] Y. Rong, Y. Hu, S. Ravishankar, H. Liu, X. Hou, Y. Sheng, A. Mei, Q. Wang, D. Li, M. Xu, J. Bisquert, H. Han, *Energy Environ. Sci.* **2017**.

[130] J. Wei, Y. Zhao, H. Li, G. Li, J. Pan, D. Xu, Q. Zhao, D. Yu, *J. Phys. Chem. Lett.* **2014**, *5*, 3937.

[131] Y. Zhao, C. Liang, H. Zhang, D. Li, D. Tian, G. Li, X. Jing, W. Zhang, W. Xiao, Q. Liu, F. Zhang, Z. He, *Energy Environ. Sci.* **2015**, *8*, 1256.

[132] C. Zhao, B. Chen, X. Qiao, L. Luan, K. Lu, B. Hu, *Adv. Energy Mater.* **2015**, *5*, 1500279.

[133] A. T. Barrows, A. J. Pearson, C. K. Kwak, A. D. F. Dunbar, A. R. Buckley, D. G. Lidzey, *Energy Environ. Sci.* **2014**, *7*, 2944.

[134] T. Zhang, S. H. Cheung, X. Meng, L. Zhu, Y. Bai, C. H. Y. Ho, S. Xiao, Q. Xue, S. K. So, S. Yang, *J. Phys. Chem. Lett.* **2017**, *8*, 5069.

[135] G. F. Samu, C. Janáky, P. V. Kamat, *ACS Energy Lett.* **2017**, *2*, 1860.

[136] S. Shao, M. Abdu-Aguye, L. Qiu, L.-H. Lai, J. Liu, S. Adjokatse, F. Jahani, M. E. Kamminga, G. H. ten Brink, T. T. M. Palstra, B. J. Kooi, J. C. Hummelen, M. Antonietta Loi, *Energy Environ. Sci.* **2016**, *9*, 2444.

[137] S. Meloni, T. Moehl, W. Tress, M. Franckevičius, M. Saliba, Y. H. Lee, P. Gao, M. K. Nazeeruddin, S. M. Zakeeruddin, U. Rothlisberger, M. Graetzel, *Nat. Commun.* **2016**, *7*, 10334.

[138] D. Bryant, S. Wheeler, B. C. O'Regan, T. Watson, P. R. F. Barnes, D. Worsley, J. Durrant, *J. Phys. Chem. Lett.* **2015**, *6*, 3190.

[139] Y. Zou, R. J. Holmes, *Adv. Energy Mater.* **2016**, *6*, 1501994.

[140] G. A. Elbaz, D. B. Straus, O. E. Semonin, T. D. Hull, D. W. Paley, P. Kim, J. S. Owen, C. R. Kagan, X. Roy, *Nano Lett.* **2017**, *17*, 1727.

[141] C. S. Ponseca, T. J. Savenije, M. Abdellah, K. Zheng, A. Yartsev, T. Pascher, T. Harlang, P. Chabera, T. Pullerits, A. Stepanov, J.-P. Wolf, V. Sundström, *J. Am. Chem. Soc.* **2014**, *136*, 5189.

[142] J. H. Heo, D. H. Song, H. J. Han, S. Y. Kim, J. H. Kim, D. Kim, H. W. Shin, T. K. Ahn, C. Wolf, T.-W. Lee, S. H. Im, *Adv. Mater.* **2015**, *27*, 3424.

[143] W. Chen, Y. Wu, Y. Yue, J. Liu, W. Zhang, X. Yang, H. Chen, E. Bi, I. Ashraful, M. Grätzel, L. Han, *Science* **2015**, *350*, 944.

[144] J. H. Heo, H. J. Han, D. Kim, T. K. Ahn, S. H. Im, *Energy Environ. Sci.* **2015**, *8*, 1602.

[145] A. K. Jena, H.-W. Chen, A. Kogo, Y. Sanehira, M. Ikegami, T. Miyasaka, *ACS Appl. Mater. Interfaces* **2015**, *7*, 9817.

[146] E. J. Juarez-Perez, M. Wuβler, F. Fabregat-Santiago, K. Lakus-Wollny, E. Mankel, T. Mayer, W. Jaegermann, I. Mora-Sero, *J. Phys. Chem. Lett.* **2014**, *5*, 680.

[147] V. W. Bergmann, Y. Guo, H. Tanaka, I. M. Hermes, D. Li, A. Klasen, S. A. Bretschneider, E. Nakamura, R. Berger, S. A. L. Weber, *ACS Appl. Mater. Interfaces* **2016**, *8*, 19402.

[148] H. Shen, D. A. Jacobs, Y. Wu, T. Duong, J. Peng, X. Wen, X. Fu, S. K. Karuturi, T. P. White, K. Weber, K. R. Catchpole, *J. Phys. Chem. Lett.* **2017**, *8*, 2672.

[149] E. Erdenebileg, L. E. Scholz, A. Hofacker, C. Koerner, K. Leo, *Energy Technol.* **2017**, *5*.

[150] K. Majhi, L. Bertoluzzi, D. A. Keller, H.-N. Barad, A. Ginsburg, A. Y. Anderson, R. Vidal, P. Lopez-Varo, I. Mora-Sero, J. Bisquert, A. Zaban, *J. Phys. Chem. C* **2016**, *120*, 9053.

[151] P. López-Varo, J. A. Jiménez-Tejada, O. Marinov, J. E. Carceller, C. H. Chen, M. J. Deen, *Organic Electronics* **2017**, *48*, 85.

[152] P. López Varo, J. A. Jiménez Tejada, J. A. López Villanueva, M. J. Deen, *Organic Electronics* **2014**, *15*, 2536.

[153] T. Minemoto, M. Murata, *J. Appl. Phys.* **2014**, *116*, 054505.

[154] T. S. Sherkar, C. Momblona, L. Gil-Escrig, J. Ávila, M. Sessolo, H. J. Bolink, L. J. A. Koster, *ACS Energy Lett.* **2017**, *2*, 1214.

[155] T. S. Sherkar, C. Momblona, L. Gil-Escrig, H. J. Bolink, L. J. A. Koster, *Adv. Energy Mater.* **2017**, *7*, 1602432.

[156] C.-H. Chiang, C.-G. Wu, *Nat. Photon.* **2016**, *10*, 196.

[157] J. Xu, A. Buin, A. H. Ip, W. Li, O. Voznyy, R. Comin, M. Yuan, S. Jeon, Z. Ning, J. J. McDowell, P. Kanjanaboos, J.-P. Sun, X. Lan, L. N. Quan, D. H. Kim, I. G. Hill, P. Maksymovych, E. H. Sargent, *Nat. Commun.* **2015**, *6*, 7081

[158] A. H. Ip, L. N. Quan, M. M. Adachi, J. J. McDowell, J. Xu, D. H. Kim, E. H. Sargent, *Appl. Phys. Lett.* **2015**, *106*, 143902.

[159] C. Tao, S. Neutzner, L. Colella, S. Marras, A. R. Srimath Kandada, M. Gandini, M. D. Bastiani, G. Pace, L. Manna, M. Caironi, C. Bertarelli, A. Petrozza, *Energy Environ. Sci.* **2015**, *8*, 2365.

[160] Y. Yuan, J. Huang, *Acc. Chem. Res.* **2016**, *49*, 286.

[161] Y. Shao, Y. Fang, T. Li, Q. Wang, Q. Dong, Y. Deng, Y. Yuan, H. Wei, M. Wang, A. Gruverman, J. Shield, J. Huang, *Energy Environ. Sci.* **2016**, *9*, 1752.

[162] Q. Chen, H. Zhou, T.-B. Song, S. Luo, Z. Hong, H.-S. Duan, L. Dou, Y. Liu, Y. Yang, *Nano Lett.* **2014**, *14*, 4158.

[163] J.-H. Im, I.-H. Jang, N. Pellet, M. Grätzel, N.-G. Park, *Nat. Nano.* **2014**, *9*, 927.

[164] J. Burschka, N. Pellet, S. J. Moon, R. Humphry-Baker, P. Gao, M. K.

Nazeeruddin, M. Gratzel, *Nature* **2013**, *499*, 316.

[165] Z. Xiao, Q. Dong, C. Bi, Y. Shao, Y. Yuan, J. Huang, *Adv. Mater.* **2014**, *26*, 6503.

[166] W. Nie, H. Tsai, R. Asadpour, J.-C. Blancon, A. J. Neukirch, G. Gupta, J. J. Crochet, M. Chhowalla, S. Tretiak, M. A. Alam, H.-L. Wang, A. D. Mohite, *Science* **2015**, *347*, 522.

[167] W. Peng, L. Wang, B. Murali, K.-T. Ho, A. Bera, N. Cho, C.-F. Kang, V. M. Burlakov, J. Pan, L. Sinatra, C. Ma, W. Xu, D. Shi, E. Alarousu, A. Goriely, J.-H. He, O. F. Mohammed, T. Wu, O. M. Bakr, *Adv. Mater.* **2016**, *28*, 3383.

[168] V. V. Kharton, A. P. Viskup, A. A. Yaremchenko, R. T. Baker, B. Gharbage, G. C. Mather, F. M. Figueiredo, E. N. Naumovich, F. M. B. Marques, *Solid State Ionics* **2000**, *132*, 119.

[169] H. Tan, A. Jain, O. Voznyy, X. Lan, F. P. García de Arquer, J. Z. Fan, R. Quintero-Bermudez, M. Yuan, B. Zhang, Y. Zhao, F. Fan, P. Li, L. N. Quan, Y. Zhao, Z.-H. Lu, Z. Yang, S. Hoogland, E. H. Sargent, *Science* **2017**, *355*, 722.

[170] J. H. Heo, M. S. You, M. H. Chang, W. Yin, T. K. Ahn, S.-J. Lee, S.-J. Sung, D. H. Kim, S. H. Im, *Nano Energy* **2015**, *15*, 530.